



Phase-field modeling of epitaxial growth: Applications to step trains and island dynamics

Zhengzheng Hu^a, John S. Lowengrub^{b,*}, Steven M. Wise^c, Axel Voigt^d

^a Department of Mathematics, North Carolina State University, Raleigh, NC 27695-8205, USA

^b Department of Mathematics, University of California, Irvine, CA 92697-3875, USA

^c Department of Mathematics, University of Tennessee, Knoxville, TN 37996-1300, USA

^d Institut für Wissenschaftliches Rechnen, Technische Universität Dresden, D-01062, Germany

ARTICLE INFO

Article history:

Received 19 January 2010

Received in revised form

6 September 2011

Accepted 6 September 2011

Available online 17 September 2011

Communicated by M. Brenner

Keywords:

Phase field

Edge diffusion

Ehrlich–Schwoebel effect

Morphological instability

Step flow

Epitaxial growth

ABSTRACT

In this paper, we present a new phase-field model including combined effects of edge diffusion, the Ehrlich–Schwoebel barrier, deposition and desorption to simulate epitaxial growth. A new free energy function together with a correction to the initial phase variable profile is used to efficiently capture the morphological evolution when a large deposition flux is imposed. A formal matched asymptotic analysis is performed to show the reduction of the phase-field model to the classical sharp interface Burton–Cabrera–Frank model for step flow when the interfacial thickness vanishes. The phase-field model is solved by a semi-implicit finite difference scheme, and adaptive block-structured Cartesian meshes are used to dramatically increase the efficiency of the solver. The numerical scheme is used to investigate the evolution of perturbed circularly shaped small islands. The effect of edge diffusion is investigated together with the Ehrlich–Schwoebel barrier. We also investigate the linear and nonlinear regimes of a step meandering instability. We reproduce the predicted scaling law for the growth of the meander amplitude, which was based on an analysis of a long wavelength regime. New nonlinear behavior is observed when the meander wavelength is comparable to the terrace width. In particular, a previously unobserved regime of coarsening dynamics is found to occur when the meander wavelength is comparable to the terrace width.

© 2011 Elsevier B.V. All rights reserved.

1. Introduction

Thin film growth through for example, molecular beam epitaxy (MBE), liquid phase epitaxy (LPE) and chemical vapor deposition (CVD) is a modern technology of growing single crystals that inherit atomic structures from a substrate [1]. Epitaxial growth produces almost defect-free, high quality crystals, which have wide ranges of applications in electronic, optical and magnetic materials. For example, epitaxial growth is useful in the manufacture of reflective or anti-reflective coatings for optics, and is important in the fabrication of layers of insulators and semiconductors for integrated circuits (e.g. see [2]). Moreover, epitaxial growth can be used to create structures on much smaller length scales through self-assembly, that is the nanostructure emerges spontaneously, rather than structures produced by top-down methods. Examples include quantum dots and quantum

wires which have very good transport and optical properties, and therefore have specific importance in the development of diode lasers, amplifiers, biological sensors and etc. (e.g. see [3,4]). The fundamental problem in epitaxial growth is to understand growth processes so that one can develop techniques to control nanostructure formation and promote self-assembly of spatially ordered nanostructures.

During epitaxial growth, physical and chemical processes occur at widely varying length and time scales. Examples of such phenomena include, the chemical interaction of the film and substrate; the heteroepitaxial misfit between substrate and film; the formation of defects, such as dislocations and grain boundaries; the extreme elastic heterogeneity of the system; the strong elastic and surface anisotropies; interface kinetic effects; epilayer deposition; edge diffusion; substrate topographical patterning and subsurface implant patterning. These processes interact and compete to form complex thin film morphologies, such as step structures, and faceted quantum dots and wires. Given such a complex multi-scale problem, modeling epitaxial growth presents an enormous challenge to mathematicians, theoretical physicists and materials scientists. Since the macroscopic evolution of the growing film is directly related to the movements of adatoms

* Corresponding author.

E-mail addresses: zhu4@ncsu.edu (Z. Hu), lowengrub@math.uci.edu (J.S. Lowengrub), swise@math.utk.edu (S.M. Wise), Axel.Voigt@tu-dresden.de (A. Voigt).

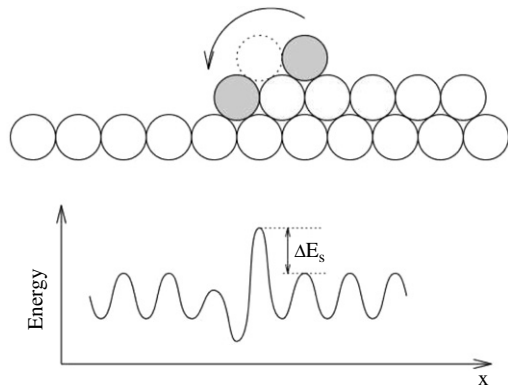


Fig. 1. Schematic of Ehrlich–Schwoebel barrier. An adatom detaching from a step edge is experiencing an additional energy ΔE_s [30].

(absorbed atoms) on surfaces and their various interactions, it is appealing to use atomic scale simulations for a theoretical description of epitaxial growth (e.g., ab-initio [5] molecular dynamics [6] and kinetic Monte Carlo [7–9] models). However, the length and time scales that can be achieved by the atomic scale simulations are limited, thus semi-discrete step-flow models (e.g., [10–15]) and continuum models (e.g., [16–27]) may be used in order to study various applications at larger scales.

Below the roughening temperature, steps as long-lived surface defects are suitable as a basis for the description of the surface morphology. Atomic steps separate exposed lattice terraces that differ in height by a single lattice spacing and provide the kink sites at which new atoms are incorporated into the crystal. The growth of a crystal surface can thus be reduced to the advancement of existing steps, the nucleation and growth of new closed step loops (i.e., atomic height islands), the annihilation of steps by the merging of islands and terraces. Burton, Cabrera and Frank (BCF) [28] first introduced a semi-discrete model, in which the growth direction is discrete but the lateral direction is continuous, to describe the diffusion of adatoms and the motion of steps during epitaxial growth of thin films. The BCF model, supplemented with later modifications and extensions, has been used to study the stability of step trains and islands.

A fundamental investigation to predict the meandering wavelength for the step meandering instability using linear stability analysis, was performed by Bales and Zangwill [10]. Their analysis shows that step meandering is an instability that may arise as a result of a terrace Ehrlich–Schwoebel barrier, see Fig. 1, which characterizes the preference of adatoms to attach to an ascending step, i.e., $k_+ < k_-$ in Eqs. (2) and (3). More recently, following Avignon and Chakraverty [13], Mullins and Sekerka [14] and Li et al. [15], a comprehensive morphological stability analysis of small circularly shaped islands was performed by Hu et al. in [29]. In this work, Hu et al. demonstrated the existence of a naturally stabilizing radius of the growing island, so that beyond this radius, the growth is always stable. Up to this radius, taking fluxes larger than a critical flux results in unstable growth. The explicit form of the dispersion relation is given in a supplementary document. Hu et al. also suggested a way of controlling the shape of an island using the deposition flux and far-field flux as control parameters. However, in the nonlinear regime, mathematical modeling and efficient numerical algorithms are essential and it remains to determine whether shape control may be achieved in the nonlinear regime.

In this paper, a new phase-field model for step flow accounting for Ehrlich–Schwoebel barrier, edge diffusion, a far-field flux, deposition and desorption, is presented and used to investigate instabilities during epitaxial growth. To accurately and efficiently capture the dynamics when the deposition flux is large, we propose a different free energy function from that used by Rätz

et al. [31] and Otto et al. [32]. An analysis using matched asymptotic expansions is performed to show that the phase-field model reduces to classical sharp interface models of BCF type when the interfacial thickness vanishes. Advantages of using a phase-field approach include the automatic capture of topological changes such as island formation, coalescence and coarsening. In addition, other physical effects such as nucleation and elastic interactions may be included. Previously, front tracking methods have been used to study the combined effects of edge diffusion and the Ehrlich–Schwoebel during island growth [33–35]. In phase field simulations [36,37] the edge diffusion term is typically neglected. Only in [2] was this effect considered, however attachment and detachment processes were neglected. In [38], a level-set method was used, where the edge diffusion term in the normal velocity was approximated by the deviation of the curvature from the averaged curvature. But none of these methods considered the combined effects of edge diffusion, the Ehrlich–Schwoebel barrier and desorption.

Moreover, to demonstrate the versatility of the proposed phase-field model, we also investigate the linear and nonlinear regimes for the step trains concentrating on the step meandering instability. A similar study has been performed by Haußer and Voigt [39] in which a front tracking method based on linear adaptive finite elements is used. In this work, we confirm some of their nonlinear results and identify a new regime of coarsening with different sets of parameters. In particular, we reproduce the predicted scaling law for the growth of the meander amplitude, which was based on an analysis of a long wavelength regime [40–42]. New nonlinear behavior is observed when the meander wavelength is comparable to the terrace width.

This paper is organized as follows: In Section 2, we describe the BCF model. In Section 3, the new phase-field model is presented. In Section 4, we briefly discuss the numerical solution of the phase-field model. In Section 5, we present and discuss our numerical results applied on both island dynamics and step trains. We give some concluding remarks and suggest some future work in Section 6. In Appendix A, a formal matched asymptotic analysis is performed to show the reduction of the phase-field model to the classical sharp interface BCF model for step flow when the interfacial thickness vanishes. The computation of the surface Laplacian is outlined in Appendix B. We present the initial condition used in the simulation of the growth under a constant flux (Section 5.1.1) in Appendix C. In Appendix D, the dispersion as appeared in [10] is presented. A supplementary document contains details of the linear stability analysis.

2. The BCF model

2.1. The BCF model for island dynamics

We consider a domain Ω on a plane containing a sequence of steps and terraces. To model island dynamics, the steps are described by closed curves Γ_i , which divide Ω into terraces Ω_i where $i = 0, \dots, N$ denotes the discrete height of the layers, cf. Fig. 2.

Let $\rho_i = \rho_i(x, y, t)$ be the adatom concentration on a terrace Ω_i , with $i = 0, \dots, N$. Then, the BCF model [28] is

$$\partial_t \rho_i - \nabla \cdot (D \nabla \rho_i) = F - \tau^{-1} \rho_i \quad \text{in } \Omega_i, \quad (1)$$

where D is the diffusion constant, F is the deposition flux rate and τ^{-1} is the desorption rate. At the step edges Γ_i , the adatom concentration satisfies the kinetic boundary conditions

$$-D \nabla \rho_i \cdot \mathbf{n}_i = k_+ (\rho_i - \rho^* (1 + \sigma \kappa_i)) \quad \text{on } \Gamma_i, \quad (2)$$

$$D \nabla \rho_{i-1} \cdot \mathbf{n}_i = k_- (\rho_{i-1} - \rho^* (1 + \sigma \kappa_i)) \quad \text{on } \Gamma_i, \quad (3)$$

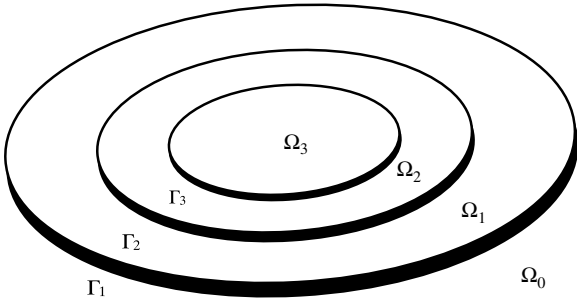


Fig. 2. Schematic of island domains, after [31].

where \mathbf{n}_i is the unit normal pointing from the upper to lower terrace, k_+ and k_- are the kinetic attachment rates from the upper and lower terraces respectively, ρ^* is the equilibrium value of the adatom concentration for a straight step, σ is the line tension and κ_i is the curvature of Γ_i .

We also assume that Ω_0 is enclosed in a large, fixed circle Γ_∞ with radius R_∞ , and an additional far-field flux J is imposed uniformly along Γ_∞

$$\frac{1}{2\pi} \int_{\Gamma_\infty} D \nabla \rho_0 \cdot \mathbf{n} d\Gamma = J \quad \text{on } \Gamma_\infty, \quad (4)$$

where \mathbf{n} is the unit exterior normal at Γ_∞ . This far-field flux could arise due to the diffusion of adatoms from other regions of the thin film as discussed in [29].

The normal velocity of a step-edge is given by

$$v_i = -D \nabla \rho_i \cdot \mathbf{n}_i + D \nabla \rho_{i-1} \cdot \mathbf{n}_i + \nabla_{s_i} \cdot (\nu \nabla_{s_i} \kappa_i) \quad \text{on } \Gamma_i, \quad (5)$$

where ν is the edge diffusion coefficient and $\nabla_{s_i} = (I - \mathbf{n}_i \mathbf{n}_i) \nabla$ is the surface gradient. Note that Eq. (5) is a fourth-order differential equation, due to the presence of edge diffusion. We refer the reader to [28,12,1,43] for more discussion about BCF models.

Here we will focus on the case in which the evolution is quasi-steady. That is, when the time scale for adatoms diffusion is much smaller than the time scale for deposition: $l_T^2/D \ll 1/F$ where l_T is a typical terrace width. Under this assumption, Eq. (1) reduces to

$$-\nabla \cdot (D \nabla \rho_i) = F - \tau^{-1} \rho_i \quad \text{in } \Omega_i,$$

while the other equations do not change.

2.2. Nondimensionalization

Time and space are non-dimensionalized by using the diffusion time scale $t^* = R_\infty^2/D$ (assume D is constant) and the length scale $l^* = R_\infty$ which is the radius of Γ_∞ [29]. We then define the non-dimensional time and space variables as

$$\hat{t} = t/t^*, \quad \hat{l} = l/l^*.$$

We also introduce the modified adatom concentration $\omega_i = \rho_i - \rho^*$ and $\omega_{i-1} = \rho_{i-1} - \rho^* - \Psi r$, where r is the non-dimensional radial distance to the center of Ω_0 and the non-dimensional far-field flux Ψ is defined below. It follows that the non-dimensional BCF model is

$$-\hat{\Delta} \omega_i = \Lambda - \mu^2 (\omega_i + \rho^*) \quad \text{in } \hat{\Omega}_i \quad (6)$$

$$-\hat{\Delta} \omega_0 = \Lambda - \mu^2 (\omega_0 + \rho^*) + \Psi \left(\frac{1}{r} - \mu^2 r \right) \quad \text{in } \hat{\Omega}_0 \quad (7)$$

$$-\xi_+ \hat{\nabla} \omega_i \cdot \mathbf{n}_i = \omega_i - \rho^* \delta \hat{\kappa}_i \quad \text{on } \hat{\Gamma}_i \quad (8)$$

$$\xi_- \hat{\nabla} \omega_{i-1} \cdot \mathbf{n}_i = \omega_{i-1} - \rho^* \delta \hat{\kappa}_i \quad \text{on } \hat{\Gamma}_i \quad (9)$$

$$\xi_- \hat{\nabla} \omega_0 \cdot \mathbf{n}_1 = \omega_0 - \rho^* \delta \hat{\kappa}_1 + \Psi (R_1 - \xi_-) \quad \text{on } \hat{\Gamma}_1 \quad (10)$$

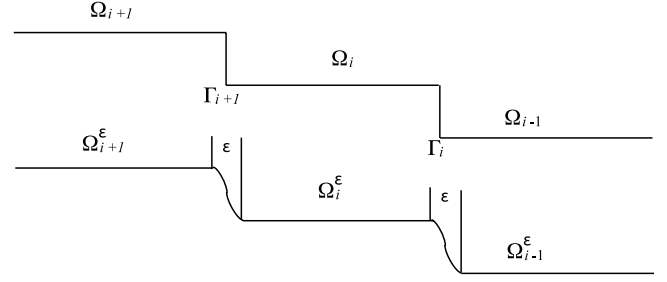


Fig. 3. Diagram of terraces (top) and the phase-field variable (bottom).

$$\frac{1}{2\pi} \int_{\hat{\Gamma}_\infty} \hat{\nabla} \omega_0 \cdot \mathbf{n} d\hat{\Gamma} = 0, \quad \text{on } \hat{\Gamma}_\infty = 1 \quad (11)$$

$$\hat{v}_i = -\hat{\nabla} \omega_i \cdot \mathbf{n}_i + \hat{\nabla} \omega_{i-1} \cdot \mathbf{n}_i + \hat{\nabla}_{s_i} \cdot (\beta \hat{\nabla}_{s_i} \hat{\kappa}_i) + \Psi \delta_{i1} \quad \text{on } \hat{\Gamma}_i \quad (12)$$

for $i = 1, \dots, N$. Here R_1 is the radius of Ω_1 , and δ_{i1} is the Kronecker delta function ($\delta_{i1} = 1$ if $i = 1$ and $\delta_{i1} = 0$ otherwise). Note that ω_i and ω_{i-1} are already dimensionless. The non-dimensional parameters in Eqs. (6)–(12) are

$$\Lambda = \frac{FR_\infty^2}{D}, \quad \mu = \frac{R_\infty}{\sqrt{D\tau}}, \quad \xi_\pm = \frac{D}{k_\pm R_\infty},$$

$$\delta = \frac{\sigma}{R_\infty}, \quad \Psi = \frac{J}{D}, \quad \beta = \frac{\nu}{DR_\infty},$$

which are non-dimensional measures of the deposition flux, the desorption rate, the attachment rates, the line tension, the far-field flux and the edge diffusion, respectively.

For simplicity, we will drop the hat notation in Eqs. (6)–(12) to refer to the non-dimensional model from now on.

3. Phase-field formulation

In the phase-field approach, the island boundaries are treated as diffuse interfaces with thickness $O(\epsilon^*)$, in order to match the non-dimensional model, we use a non-dimensional thickness $\epsilon = \epsilon^*/l^*$. Both islands and lower terraces can be viewed as separate phases of the system and accordingly are described by a phase-field variable $\phi^\epsilon = \phi^\epsilon(x, y, t; \epsilon)$, cf. Fig. 3. The phase function ϕ^ϵ also can be interpreted as a continuous approximation of the discrete height function of the growing film. By extending the model of Rätz et al. [31], we present a new 6-th order phase-field model to account for edge diffusion and a far-field flux:

$$\begin{aligned} \partial_t \phi^\epsilon - \nabla_s \cdot (\beta \nabla_s \kappa) |\nabla \phi^\epsilon| \\ = \nabla \cdot (M(\phi^\epsilon, \epsilon) \nabla (\omega^\epsilon + K(\phi^\epsilon, r; \epsilon))) \\ + \Lambda - \mu^2 (\omega^\epsilon + K(\phi^\epsilon, r; \epsilon) + \rho^*), \end{aligned} \quad (13)$$

$$\begin{aligned} \alpha \epsilon^2 (\partial_t \phi^\epsilon - \nabla_s \cdot (\beta \nabla_s \kappa) |\nabla \phi^\epsilon|) \\ = \epsilon^2 \Delta \phi^\epsilon - G'(\phi^\epsilon) + \frac{\epsilon}{\rho^* \delta} (\omega^\epsilon + K(\phi^\epsilon, r; \epsilon)), \end{aligned} \quad (14)$$

where $\omega^\epsilon = \omega^\epsilon(x, y, t; \epsilon)$ is the approximated modified adatom density and κ is the curvature and can be calculated by $-\nabla \cdot \frac{\nabla \phi^\epsilon}{|\nabla \phi^\epsilon|}$.

In the following sections we will drop superscript ϵ and use ω and ϕ in the phase-field model. In Eqs. (13) and (14), the Hamilton–Jacobi like term $\nabla_s \cdot (\beta \nabla_s \kappa) |\nabla \phi|$ accounts for the effects of edge diffusion and $M(\phi, \epsilon)$ is the anisotropic mobility that models the Ehrlich–Schwoebel barrier. The function $K(\phi, r; \epsilon) = \Psi \prod_{j=1}^N (1 - \phi/j)r$ is used to account the far-field flux, and vanishes on all terraces except for on Ω_0 , i.e., $\phi = 0$. The parameter α is introduced in order to match the sharp interface model as shown

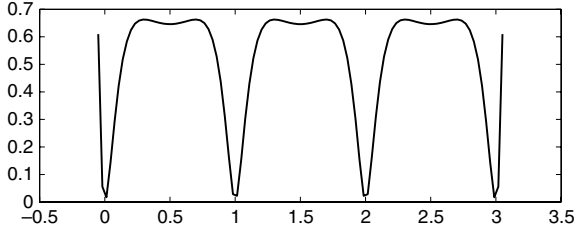


Fig. 4. The multiwell potential $G(\phi)$ from Eq. (15).

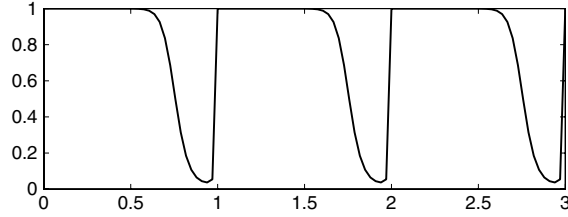


Fig. 5. The asymmetric mobility function $M(\phi, \epsilon)$ from Eq. (16).

in Eq. (17) (see [31] and Appendix A for more details). The function $G(\phi)$ is a multi-well free energy function, cf. Fig. 4,

$$G(\phi) = b(e^{f(i)} - 1)(e^{f(i+1)} - 1), \quad \text{for } \phi \in [i, i+1], \quad (15)$$

where $f(i) = 4.5(i - \phi)^2 + 0.9(i - \phi)^4$ and b is a scaling factor such that $\int_i^{i+1} \sqrt{2G(\phi)} d\phi = 1$ for $i = 0, \dots, N-1$. Note that $G(\phi + 1) = G(\phi)$ for $\phi \in [0, N-1]$ and $G(\phi)$ has the symmetry $G(i + 1/2 + \phi) = G(i + 1/2 - \phi)$ for $i = 0, \dots, N-1$. This energy function is different from the standard polynomial free energy that was used in [31]. We will show in Section 5 that this specific form of energy function helps to more accurately model the adatom mobility on the terraces when the deposition flux is large. To account for the Ehrlich–Schwoebel barrier, the mobility is asymmetric [31], cf. Fig. 5,

$$M(\phi, \epsilon) = \frac{1}{1 + \epsilon^{-1}\zeta(\phi)} \quad (16)$$

where $\zeta(\phi) = \gamma(\phi - (i-1))^p G(\phi)$ when $\phi \in [i-1, i]$ for $i = 1, \dots, N$. Here, as shown in Eq. (A.37), γ and p satisfy

$$\int_{i-1}^i \frac{\zeta(\phi)}{\sqrt{2G(\phi)}} (1-\phi) d\phi = \xi_-, \quad \int_{i-1}^i \frac{\zeta(\phi)}{\sqrt{2G(\phi)}} \phi d\phi = \xi_+.$$

The interfaces are now defined by

$$\Gamma_i(\epsilon) := \left\{ (x, y) \in \Omega : \phi(x, y, t; \epsilon) = i - \frac{1}{2} \right\}, \quad i = 1, \dots, N.$$

We will show in Appendix A that in the asymptotic limit, i.e., $\epsilon \rightarrow 0$, taking

$$\alpha = \frac{1}{\rho^* \delta} \int_0^1 \frac{\zeta(\phi)}{\sqrt{2G(\phi)}} (1-\phi) \phi d\phi, \quad (17)$$

the phase-field model (Eqs. (13)–(14)) reduces to the quasi-steady BCF model (Eqs. (6)–(12)) accounting for Ehrlich–Schwoebel barrier, edge diffusion, a far-field flux, deposition and desorption.

4. Numerical solutions

In this section we discuss a numerical algorithm to solve the phase-field model. We use semi-implicit time and centered difference space discretizations on Eqs. (13) and (14). Following Smereka [44], we introduce a smoothing method originally developed for a level-set method to efficiently calculate the edge

diffusion term. Basically, two bi-Laplacians ($\Delta^2 \phi$) are added and subtracted from the equations in which the edge diffusion appears. Defining $\varrho := \omega + K(\phi, r; \epsilon)$ and $\varpi := \Delta \phi$, we present our numerical scheme as follows:

$$\begin{aligned} & \frac{\phi_{ij}^{k+1} - \phi_{ij}^k}{\Delta t} - \nabla_s \cdot (\beta \nabla_s \kappa_{ij}^k) |\nabla \phi_{ij}^k| + \vartheta \Delta \varpi_{ij}^{k+1} \\ & = \nabla_d \cdot (M_{ij}^{k+\frac{1}{2}} \nabla_d \varrho_{ij}^{k+\frac{1}{2}}) + \Lambda - \mu^2 (\varrho_{ij}^{k+\frac{1}{2}} + \rho^*) + \vartheta \Delta \varpi_{ij}^k \end{aligned} \quad (18)$$

$$\begin{aligned} & \alpha \epsilon^2 \left(\frac{\phi_{ij}^{k+1} - \phi_{ij}^k}{\Delta t} - \nabla_s \cdot (\beta \nabla_s \kappa_{ij}^k) |\nabla \phi_{ij}^k| + \vartheta \Delta \varpi_{ij}^{k+1} \right) \\ & = \frac{\epsilon^2}{2} \Delta_d (\phi_{ij}^{k+1} + \phi_{ij}^k) - \frac{1}{2} (G'(\phi_{ij}^{k+1}) + G'(\phi_{ij}^k)) \frac{\epsilon}{\rho^* \delta} \varrho_{ij}^{k+\frac{1}{2}} \\ & \quad + \alpha \epsilon^2 \vartheta \Delta \varpi_{ij}^k \end{aligned} \quad (19)$$

$$\varrho_{ij}^{k+\frac{1}{2}} = \omega_{ij}^{k+\frac{1}{2}} + K_{ij}^k \quad (20)$$

$$\varpi_{ij}^{k+1} = \Delta \phi_{ij}^{k+1} \quad (21)$$

$$\kappa_{ij}^k = -\nabla \cdot \left(\frac{\nabla \phi_{ij}^k}{|\nabla \phi_{ij}^k|} \right) \quad (22)$$

where $M_{ij}^{k+\frac{1}{2}} = \frac{1}{2}(M(\phi_{ij}^{k+1}) + M(\phi_{ij}^k))$. The bi-Laplacian is added to the system as a smoothing operator and a coarse approximation of the curvature. Our study shows that taking $\vartheta = \beta/2$ results in a stable scheme at the time steps we have tested. This observation matches with Smereka's results in [44]. The computation of the surface Laplacian is outlined in Appendix B. We remark that, all terms in Eqs. (18) and (22) are second-order in time, except for the edge diffusion term and the far-field flux term. We found it is difficult to make a stable, fully second-order scheme. To efficiently solve the discrete system at the implicit time-level, we use a nonlinear multigrid method originally developed for Cahn–Hilliard equations by Kim et al. [45] for uniform grids and extended by Wise et al. [46] to adaptive block-structured Cartesian meshes. Fig. 6 shows a typical adaptive mesh generated by the solver for island dynamics simulations. We refer the reader to Trottenberg et al. [47], Kim et al. [45] and Wise et al. [46] for further details about the nonlinear FAS multigrid scheme and to Hu [48] for the applications to the Eqs. (18)–(22).

5. Applications

In this section, we apply the phase-field model developed in Section 3 to investigate the morphology of thin films during epitaxial growth. The goal is to characterize the nonlinear evolution of nanoscale islands and step trains. It is also important to determine the extent of applicability of the linear stability theory for islands developed by [29] and the more classical linear stability theory for step trains by [10]. We first present results related to island dynamics. The step trains are investigated in the next subsection.

5.1. Island dynamics

5.1.1. Growth under a constant flux

We start with a preliminary result, in which the desorption rate, edge diffusion and far-field flux are absent, and the deposition flux is constant. To simulate the growth of a circular island enclosed in a unit disk, we use $[-1, 1] \times [-1, 1]$ as the computational domain and scale the deposition flux by a cutoff function, specifically, a hyperbolic tangent function supported on the unit disk. The linear stability analysis by Hu et al. [29] indicates that instability occurs

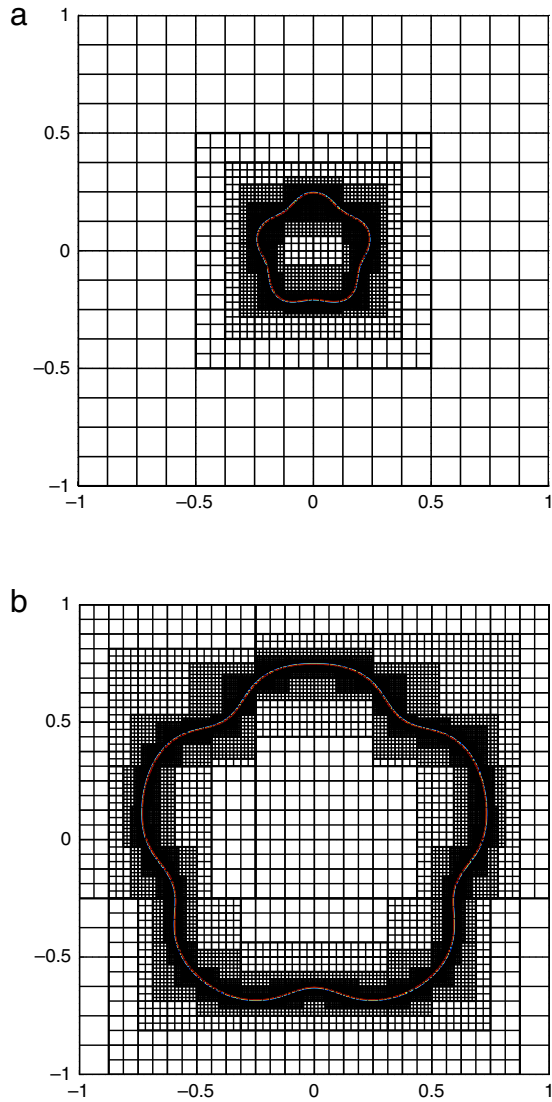


Fig. 6. Snap-shots of the adaptive block-structured Cartesian meshes at two different times during the growth of a small, perturbed circular island. There are 6 levels of refinement and all parameters are the same as those in Fig. 7.

when the deposition flux is sufficiently large. However, in order to capture the morphological evolution of the interface under large deposition fluxes, a very smaller interface thickness is required in the original phase-field model for island dynamics developed by Rätz et al. [31]. This means, even though asymptotic analysis of the model in [31] indicates convergence in ϵ , the regime of applicability requires ϵ to be very small. To make the calculations feasible and to extend the applicability of the phase-field model, we utilize the free energy $G(\phi)$ in Eq. (15) and we have also found that it is helpful to correct the hyperbolic tangent initial profile of the phase variable by adding the first order outer solution of the phase variable from the asymptotic analysis. In particular, the correction term we add is $\epsilon\phi_1$, where $\phi_1 = \frac{\omega_{\text{linear}}}{\rho^* \delta C''(\phi_0)}$, ω_{linear} is the linear solution, and ϕ_0 is the hyperbolic tangent function. The explicit expression of the initial condition is presented in Appendix C.

In Fig. 7(a), the evolution of a perturbed circular island under a constant flux is shown. The island boundary is defined by $R(\theta, 0) = R(0)(1 + P(0)\cos(5\theta))$ with radius $R(0) = 0.228$ and shape factor $P(0) = 0.087$, initially. We use $\epsilon = 0.00625$, and 7 levels of mesh refinement with $h_{\text{max}} = 1.25 \times 10^{-1}$ on the coarsest mesh and $h_{\text{min}} = 9.765625 \times 10^{-4}$ at the finest level in each coordinate

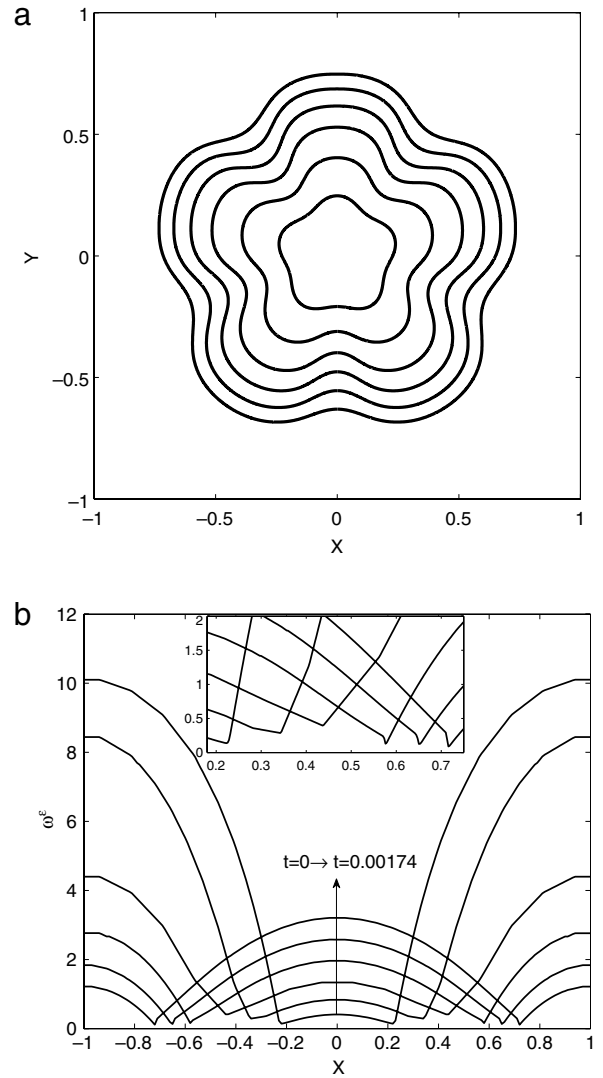


Fig. 7. (a) The evolution of a perturbed circular island under a constant deposition flux at 6 times: $t = 0$, $t = 0.0030$, $t = 0.0066$, $t = 0.0102$, $t = 0.0138$, and $t = 0.0174$. (b) Slices of the concentration field along $y = 0$ corresponding to the times shown in (a). The non-dimensional parameters are $\Lambda = 25$, $\xi_+ = 0.0256$, $\xi_- = 0.002$, $\rho^* = 1$, $\delta = 0.02$, $\beta = 0.0$, $p = 20$, $\epsilon = 6.25 \times 10^{-3}$, $\Delta t = 1 \times 10^{-7}$ and $h_{\text{min}} = 9.765625 \times 10^{-4}$.

direction. There are approximately 6 computational nodes across the island interface on the finest mesh. The time step is $\Delta t = 1 \times 10^{-7}$ and the islands are shown at non-dimensional times $t = 0$, $t = 0.0030$, $t = 0.0066$, $t = 0.0102$, $t = 0.0138$, and $t = 0.0174$. The small time step is chosen to achieve highly accurate results; the method is stable with larger time steps. As seen from the figure, the island undergoes unstable growth initially but the perturbations start to decrease as the island becomes sufficiently large. This matches the linear stability analysis result presented in [29]. The explicit expression of the dispersion relation in terms of the wave number is presented in a supplementary material. Slices of the concentration ω^ϵ at $y = 0$ are shown in Fig. 7(b). We observe in a close-up of the plot that the concentration has a near jump at the island boundary, which is consistent with the classical theory where there is a jump. Moreover, the radius of the underlying circle $R(t)$ during the evolution is plotted versus time in Fig. 8(a). The plot shows an excellent agreement between the linear theory (the solid line) and the numerical result (the dash-dotted line). To find the numerical underlying radius at time t , we first find the distance from points along the 0.5 contour

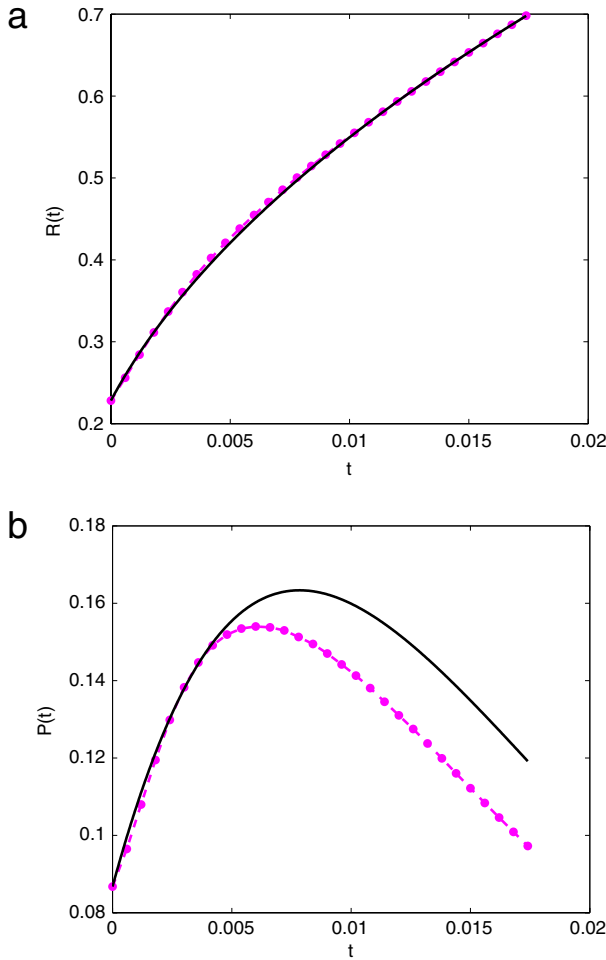


Fig. 8. (a) The radii of the underlying circle during the evolution versus time. The solid curve is the solution from linear analysis and the dash–dot line is the numerical result from Fig. 7 (see text for definition of the numerical radius). (b) The evolution of the corresponding shape factors (see text for definition) versus time. The non-dimensional parameters are $\Lambda = 25$, $\xi_+ = 0.0256$, $\xi_- = 0.002$, $\rho^* = 1$, $\delta = 0.02$, $\beta = 0.0$, $p = 20$, $\epsilon = 6.25 \times 10^{-3}$, $\Delta t = 1 \times 10^{-7}$ and $h_{min} = 9.765625 \times 10^{-4}$.

($\phi = 0.5$) and the center of the island, denoted by $d(\theta, t)$, where θ is the parametrization of the 0.5 contour. The numerical underlying radius is then $R(t) = \sqrt{\frac{1}{2\pi} \int_0^{2\pi} d^2(\theta, t) d\theta}$ and the integral is evaluated by the trapezoidal rule. In Fig. 8(b), the evolution of the shape factor $P(t)$ (the dash–dotted line) is shown. The numerical shape factor is the numerical perturbation divided by the numerical radius, where the numerical perturbation is the maximum deviation from points along the 0.5 contour relative to the numerical radius, i.e., $P(t) = \max_{\theta}(d(\theta, t))/R(t)$. We observe that the linear theory (the solid line) over-predicts the growth of the perturbation.

5.1.2. Examining the effect of the edge diffusion

We now present results accounting for the effect of edge diffusion with and without kinetic effects. We first validate the scheme by verifying convergence in interfacial thickness. Three different interfacial thicknesses are used to simulate the evolution of a perturbed circular island, and then the shape factors are calculated and compared to the linear result.

The same computational domain as in the previous example is used and the deposition flux, the far-field flux and the kinetic rates are absent, i.e., $\alpha = 0$. Initially, the island is defined by $R(\theta, 0) = R(0)(1 + P(0) \cos(5\theta))$ with radius $R(0) = 0.2$ and

shape factor $P(0) = 0.078$. We use $\epsilon_1 = 0.04$, $\epsilon_2 = 0.03$, $\epsilon_3 = 0.02$, and the corresponding mesh sizes on the finest grid are $h_1 = 2.8 \times 10^{-3}$ (two levels of refinement starting with grid size 1.1111×10^{-2} on the coarsest mesh), $h_2 = 2.0 \times 10^{-3}$ (three levels of refinement starting with grid size 1.5625×10^{-2} on the coarsest mesh), $h_3 = 1.4 \times 10^{-3}$ (three levels of refinement starting with grid size 1.1111×10^{-2} on the coarsest mesh). There are approximately 12–14 computational nodes on the finest mesh across the island interface for all cases and the time step is 1.25×10^{-7} for all three cases. In the first row of Fig. 9, the evolution of the island described above is shown for $\epsilon = 0.04$ at two non-dimensional times $t = 2.5 \times 10^{-4}$ and $t = 1.0 \times 10^{-3}$. Note for the sake of presentation, only part of the domain is shown. As seen from the plots, the perturbation of the island decays and the decaying rate matches the linear stability analysis presented in [29] as shown in Fig. 10(a). The second row in Fig. 9 shows the numerical results related to the calculation of the edge diffusion. In fact, the numerical result of $f(\phi) \nabla_s \cdot (\beta \nabla_s \kappa_{ij}^k) |\nabla \phi_{ij}^k|$ in Eq. (18) is plotted, and one should notice that the numerical result provides smooth approximation to the original expression. (See Appendix B for details about function $f(\phi)$).

In Fig. 10(a), the evolution of the shape factors $P(t)$ is shown in both linear and log scales (inset). The solid lines describe the linear prediction and the dashed lines show the numerical result. We observe from the inset, that the growth rate given by the numerical results with all three interfacial thickness match with the linear theory very well when the perturbation is not very small. When the numerical perturbation reaches the size of the truncation error, it saturates. Quantitatively, we calculate the growth rate of the shape factor for all three cases and plot the result versus ϵ in Fig. 10[b]. The growth rate of the shape factor $P(t)$ is obtained by performing a linear least square fit of $\log(P(t)/P(0))$ up to $t = 3.0 \times 10^{-3}$. The three growth rates obtained are -1218.9 for $\epsilon = 0.04$, -1164.1 for $\epsilon = 0.03$, and -1089.1 for $\epsilon = 0.02$. The dashed-line shows a best fit linear to the calculated numerical growth rates, which gives a y-intercept equals -962.7 . This y-intercept compares very well to the growth rate calculated by the linear stability analysis which equals -970.5 . Fig. 10[b] also implies first-order convergence of the growth rate in the interfacial thickness.

When kinetics and edge diffusion are present, the phase-field model is indeed sixth-order. Our numerical simulation still matches the linear theory well as shown in Fig. 11. In Fig. 11, the evolution of the shape factors $P(t)$ when kinetics is present is shown in both linear and log-linear scales (inset). Again the solid lines describe the linear prediction and the dashed lines indicate the numerical result.

5.1.3. Demonstrating the idea of shape control

Following the shape control idea presented by Hu et al. in [29], we simulate the growth of a circular island perturbed with 3 modes under a variable deposition flux (cf. Fig. 12(b)). The modes included initially are $l = 3$, $l = 5$, $l = 8$ and the deposition flux is varying in time such that it always amplifies $l = 5$ most according to the linear theory presented in [29]. As seen from Fig. 12(a), the growth of the 5th-mode ($l = 5$) dominates among all the modes toward the end of the evolution. This implies that this variable deposition flux obtained through the linear stability analysis, can provide a good approximation to the actual deposition flux needed in the nonlinear simulation.

5.2. Step trains

We now move on to the step trains. On a vicinal (stepped) surface with straight, equidistant steps, either the surface separates into regions of high step density (step bunches) and wide terraces, or the steps become wavy (step meandering). In this section, we concentrate on the step meandering instability due to the

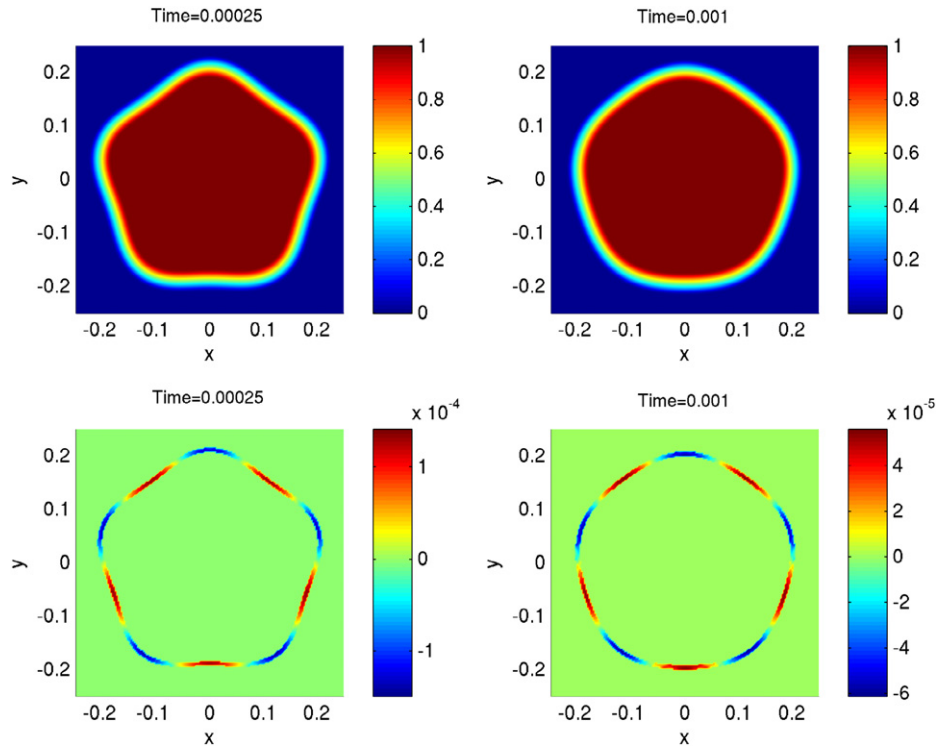


Fig. 9. The evolution of a perturbed circular island with edge diffusion, but no interface kinetics, at times: $t = 0.00025$, and $t = 0.001$. Top row: the numerical phase variable ϕ is plotted, where the value 1 indicates the island, and the value 0 indicates the lower terrace. Bottom row: the numerical result related to the calculation of the edge diffusion is plotted, see the text for a description. The non-dimensional parameters are $\Lambda = 0$, $\xi_+ = 0.027$, $\xi_- = 0.002$, $\rho^* = 1$, $\delta = 0.03$, $\beta = 0.001$, $p = 20$, $\epsilon = 0.03$, $\Delta t = 1.25 \times 10^{-7}$ and $h_{min} = 2.8 \times 10^{-3}$.

Ehrlich–Schwoebel (ES) barrier. We note that none of the instabilities presented here occur in the absence of the ES barrier.

Similar to the island dynamics model described in Section 2, we consider a domain Ω on a plane containing a sequence of steps and terraces in which the steps are described by curves Γ_i (need not to be closed), cf. the top graph in Fig. 3. The only assumption that differs from the island dynamics model in Section 2, is the far-field boundary condition. More specifically, we assume the adatom density is periodic in both horizontal and vertical directions. It then follows that the non-dimensional BCF equations for step trains are

$$-\hat{\Delta}\rho_i = \Lambda - \mu^2\rho_i, \quad \text{in } \hat{\Omega}_i(\hat{t}) \quad (23)$$

$$-\xi_+\hat{\nabla}\rho_i \cdot \mathbf{n}_i = \rho_i - \rho^*(1 + \delta\hat{\kappa}_i) \quad \text{on } \hat{\Gamma}_i(\hat{t}) \quad (24)$$

$$\xi_-\hat{\nabla}\rho_{i-1} \cdot \mathbf{n}_i = \rho_{i-1} - \rho^*(1 + \delta\hat{\kappa}_i) \quad \text{on } \hat{\Gamma}_i(\hat{t}) \quad (25)$$

$$\hat{V}_i = -\hat{\nabla}\rho_i \cdot \mathbf{n}_i + \hat{\nabla}\rho_{i-1} \cdot \mathbf{n}_i + \hat{\nabla}_{\hat{s}_i} \cdot (\beta\hat{\nabla}_{\hat{s}_i}\hat{\kappa}_i) \quad \text{on } \hat{\Gamma}_i(\hat{t}). \quad (26)$$

Here all variables and nondimensional parameters are defined as in Section 2.2.

5.2.1. Linear stability results for step meandering

Through a linear stability analysis, Bales and Zangwill [10] first showed that ES barrier induces step meandering that is, straight steps are susceptible to instabilities. Because of an effective step–step repulsion, the meander can be most easily accommodated if the steps meander in phase. In the context of the linear analysis, this means that the in-phase meander is the mode with the largest growth rate. The growth rate $\omega(\ell)$ in terms of the wave number ℓ is presented in Appendix D for the case without desorption. Following the analysis in [29], setting $\frac{\partial\omega(\ell)}{\partial\ell} = 0$, and solving for the flux Λ , we find a flux Λ_m which uniquely determines the most unstable wavelength λ_m . The explicit form of such flux is presented in a supplementary material.

5.2.2. Phase-field model revisited for step trains

We present the phase-field formulation for the step trains without the far-field flux as follows:

$$\begin{aligned} \partial_t\phi^\epsilon - \nabla_s \cdot (\beta\nabla_s k)|\nabla\phi^\epsilon| \\ = \nabla \cdot (M(\phi^\epsilon, \epsilon)\nabla\rho^\epsilon) + \Lambda - \mu^2\rho^\epsilon \end{aligned} \quad (27)$$

$$\begin{aligned} \epsilon\epsilon^2(\partial_t\phi^\epsilon - \nabla_s \cdot (\beta\nabla_s k)|\nabla\phi^\epsilon|) \\ = \epsilon^2\Delta\phi^\epsilon - G'(\phi^\epsilon) + \frac{\epsilon}{\rho^*\delta}(\rho^\epsilon - \rho^*) \end{aligned} \quad (28)$$

where $\rho^\epsilon = \rho^\epsilon(x, y, t; \epsilon)$ is the approximated adatom density.

To simulate an infinite step train, we assume that ρ^ϵ is periodic in both coordinates and ϕ^ϵ is quasi-periodic, i.e., ϕ^ϵ is periodic in the y -direction and in the x -direction $\phi^\epsilon(x_{\text{left}}, y) = \phi^\epsilon(x_{\text{right}}, y) + N$, in which the computational domain is defined as $[x_{\text{left}}, x_{\text{right}}] \times [y_{\text{down}}, y_{\text{up}}]$, and N is the total number of steps. Under this assumption, as a step moves out of the domain at the right, it re-enters the domain from the left and grows in height by one atomic level.

5.2.3. Match to the linear stability result

We first use linear stability theory to validate the numerical scheme. To this end we consider a periodic step placed in a quasi-periodic domain defined by $[-0.5, 0.5] \times [-2, 2]$. In this setup, the terrace width is equal to the domain width $L = 1$. Using the parameters $\delta = 0.03$, $\rho^* = 1.0$, $\xi_- = 0.1$, $\xi_+ = 1.0$, $\beta = 0$, we find the flux such the most unstable wavelength $\lambda_m = 4$ is $\Lambda_m = 0.624782$. Computationally, $\Delta t = 2 \times 10^{-4}$ and $\epsilon = 0.03$. We use 3 levels of mesh refinement with grid size $h_{\text{max}} = 3.125 \times 10^{-2}$ on the coarsest mesh and grid size $h_{\text{min}} = 3.90625 \times 10^{-3}$ on the finest level. There are approximately 6 computational nodes across the interface on the finest mesh. The straight step is initially perturbed by small amplitudes with two different wavelengths: $\lambda = 4$ and $\lambda = 1$. As shown in Fig. 13(a), the steps synchronize

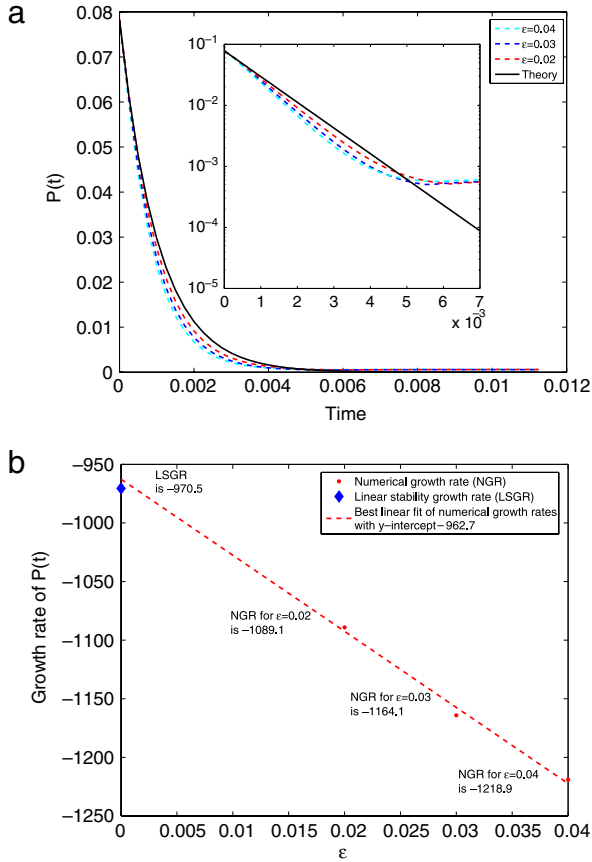


Fig. 10. (a) The evolution of the shape factor versus time for three different interfacial thickness. In the inset, the y-axis is shown in log scale whereas the x-axis is shown in linear scale. (b) The numerical growth rate of the shape factor $P(t)$ for three different interfacial thicknesses is plotted versus ϵ (red dots). The growth rate obtained by the linear stability provided in [29] is shown in a diamond mark. The dashed line is the best linear fit of numerical growth rates. See text for more description. The non-dimensional parameters are $\Lambda = 0$, $\xi_+ = 0.0$, $\xi_- = 0.0$, $\rho^* = 1$, $\delta = 0.03$, $\beta = 0.001$, $p = 20$, $\Delta t = 1.25 \times 10^{-7}$, $h_{min} = 2.8 \times 10^{-3}$ ($\epsilon = 0.04$), $h_{min} = 2.0 \times 10^{-3}$ ($\epsilon = 0.03$) and $h_{min} = 1.4 \times 10^{-3}$ ($\epsilon = 0.02$). (For interpretation of the references to colour in this figure legend, the reader is referred to the web version of this article.)

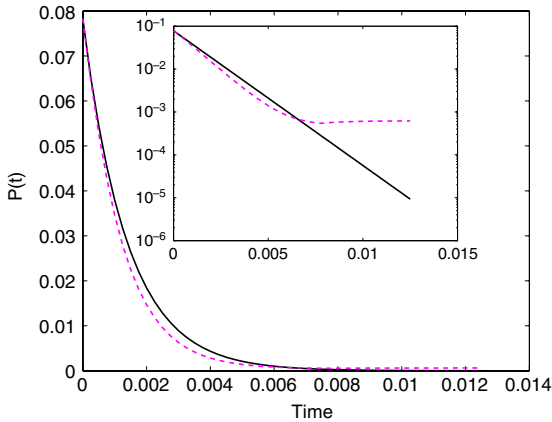


Fig. 11. The evolution of the shape factor versus time for the case in which both the edge diffusion and kinetics are present (log-linear scale is shown in the inset). The non-dimensional parameters are $\Lambda = 0$, $\xi_+ = 0.027$, $\xi_- = 0.002$, $\rho^* = 1$, $\delta = 0.03$, $\beta = 1 \times 10^{-4}$, $p = 20$, $\epsilon = 0.03$, $\Delta t = 1.25 \times 10^{-8}$ and $h_{min} = 9.765625 \times 10^{-4}$.

very quickly and then meander with a growth rate that coincides very well with the linear stability theory as seen in Fig. 13(b). In

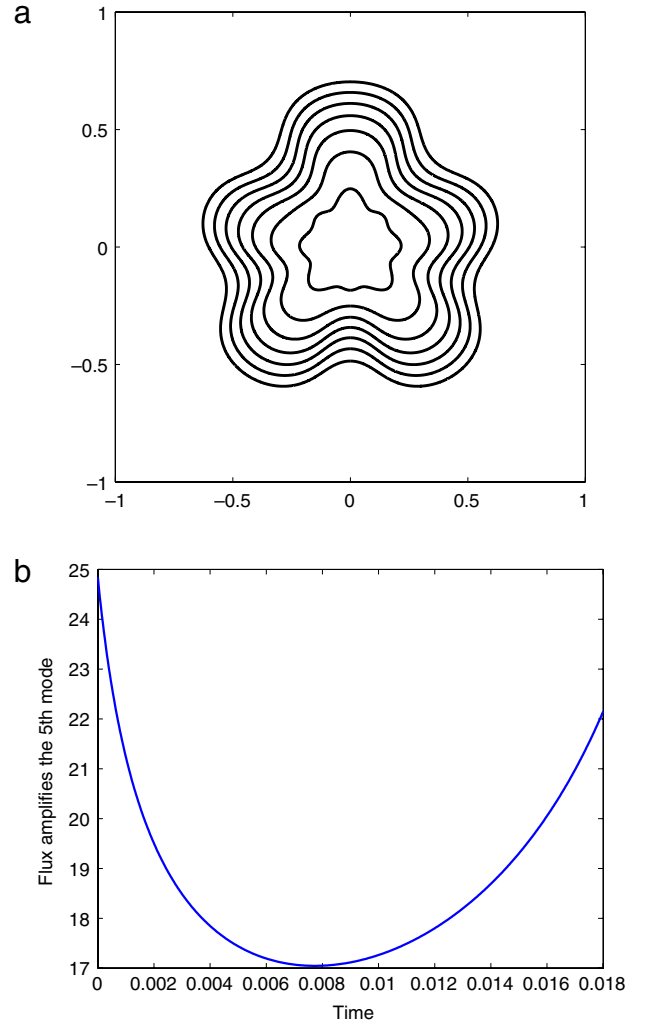


Fig. 12. Controlling the shape of a small island with deposition flux. (a). The evolution an initially perturbed island under a variable deposition flux which maximizes the growth of the 5-th mode. The 0.5 contour lines of the phase-variable are shown at 7 different times: $t = 0$, $t = 0.003$, $t = 0.006$, $t = 0.009$, $t = 0.012$, $t = 0.015$ and $t = 0.018$. (b). The variable deposition flux, which is used to control the shape of the island is plotted versus time. The non-dimensional parameters are $\xi_+ = 0.0256$, $\xi_- = 0.002$, $\rho^* = 1$, $\delta = 0.02$, $\beta = 0.0$, $p = 20$, $\epsilon = 1.25 \times 10^{-2}$, $\Delta t = 2 \times 10^{-7}$ and $h_{min} = 9.765625 \times 10^{-4}$.

Fig. 13(b) the amplitude of the step perturbation is plotted as a function of time in a log-linear scale. The predicted growth rate based on the numerical data is about 0.127852 which matches with the linear theory (Eq. (D.1), $\omega(2\pi/4, \Lambda_m) = 0.127853$) very well. To determine the numerical perturbation amplitude, we first find the mean of the interface position. This is done by averaging of the x -coordinate of all points on the 0.5 contour line of the phase variable ϕ . The amplitude is the maximum deviation from all points along the 0.5 contour line relative to the interface mean.

5.2.4. Meandering in the long wavelength regime

Having validated the numerical method with linear stability theory, we next turn to the nonlinear evolution. We first consider the case in which the most unstable wavelength is much longer than the inter-terrace distance: $\lambda_m/L = 4$. We used the exact same computational domain, initial data and parameters as those in Section 5.2.3. To access the nonlinear region, the simulation was run to a much longer time $t = 200$; the results are shown in Fig. 14. We observe: (i) endless growth of the amplitude, (ii) the forward and the backward meander are no longer

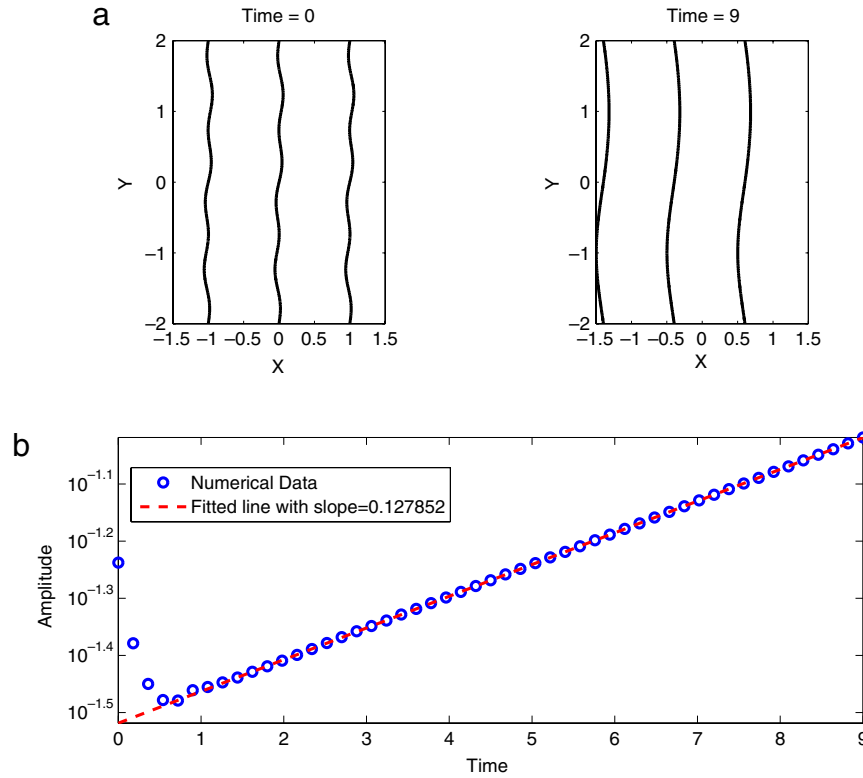


Fig. 13. The time evolution of a perturbed step train. The step moves from left to right and the lower terrace is always on the right. Note that 3 periods are shown in x -direction. (a) The 0.5 contour lines of the step at different times. The instability adopts the most unstable wavelength $\lambda_m = 4$. (b) The amplitude (see text for definition) of the interface is plotted versus time in log-linear scale. The fitted growth rate is 0.127852 which compares very well with the linear theory value 0.127853. The parameters are $\delta = 0.03$, $\rho^* = 1.0$, $\xi_- = 0.1$, $\xi_+ = 1.0$, $\beta = 0$, $A = 0.624782$, $L = 1$, domain $[-0.5, 0.5] \times [-2, 2]$, $\epsilon = 0.03$, $\Delta t = 2 \times 10^{-4}$ and $h_{min} = 3.90625 \times 10^{-3}$.

symmetric, and (iii) the backward meander creates a region with finite slope, which is defined as a plateau by Gillet et al. [41]. Also, we find out that at the late stage, the growth rate of the amplitude is $t^{0.4981}$. These results quantitatively match with Pierre-Louis et al. [40–42], in which the growth rate is predicted to be $t^{0.5}$ based on a local amplitude equation. A qualitatively similar result was also observed by Haußer & Voigt [39].

5.2.5. Meandering in the short wavelength regime

We now move on to the regime in which the most unstable wavelength is comparable to the inter-terrace distance. In this case, the nonlinear behavior of steps is not predictable by the local amplitude equation.

- **Existence of a steady-state.** In Fig. 15, the parameters are selected such that the most unstable wavelength $\lambda_m = 1$ and is equal to the inter-terrace distance, i.e. $L/\lambda_m = 1$. At early times, the growth of the amplitude follows the prediction given by the linear stability theory, but starts to level off and reaches to a steady state at late times. We remark that, Haußer & Voigt [39] reported the existence of a steady-state when the most unstable wavelength is much smaller than the inter-terrace distance (i.e., $L/\lambda_m = 5$) and $\xi_+/\xi_- = 100$ which is 10 times bigger than what we used.
- **Formation of a vacancy island.** Using the same L/λ_m ratio, one may observe a different morphology if a large amplitude is assumed initially. Taking the same parameters as in Fig. 15, the evolution from a large amplitude initial condition is shown in Fig. 16. We observe the formation of a mushroom, pinch off, and the appearance of a vacancy island. Shortly after the island forms, it fills due to the adatom attachment from deposition and diffusion on the terraces. Finally growth is

stabilized. We remark that Haußer & Voigt [39] observed a similar morphological evolution. Since they used a front-tracking method which breaks down at pinch-off, they did not report the behavior following by the pinch-off. Other initial amplitudes were also simulated, and we found that at the final stage, the amplitude tends to stabilize at the same value independent of the initial amplitude, though the dynamics to reach the steady-state could be dramatically different. More specifically, the final amplitude for the case showing in Fig. 16 is the same as the case showing in Fig. 15, and the value is around 0.15.

- **Coarsening.** Lastly, we report the existence of coarsening due to competition among different wavelengths. The initial condition we adopt is a perturbed sinusoidal curve with two different wavelengths: $\lambda_1 = 1$ and $\lambda_2 = 4$, and the inter-terrace distance is $L = 1$. The parameters have been chosen such that the most unstable wavelength is $\lambda_m = \lambda_1 = 1$. As seen in Fig. 17(a), coarsening may occur in the nonlinear regime. In Fig. 17(a), two backward meanders (areas with negative amplitude relative to the center of the step) join with one forward meander (areas with positive amplitude relative to the center of the step) and form a new backward meander. This is comparable to the finding by Haußer & Voigt [50] in their study of geometric Ginzburg–Landau theory for faceted crystals, in which they reported coarsening via kink–anti-kink–kink coalescence. The kinks are the backward meanders and the antikinks are the forward meanders. We think the coarsening is due to the competition of two wavelengths in the nonlinear regime. Recall that in Section 5.2.5, we showed that the growth of $\lambda_1 = \lambda_m = 1$ will become steady in the nonlinear regime. In Fig. 17(b), the blue curve with circles depicts the growth of $\lambda_1 = \lambda_m =$

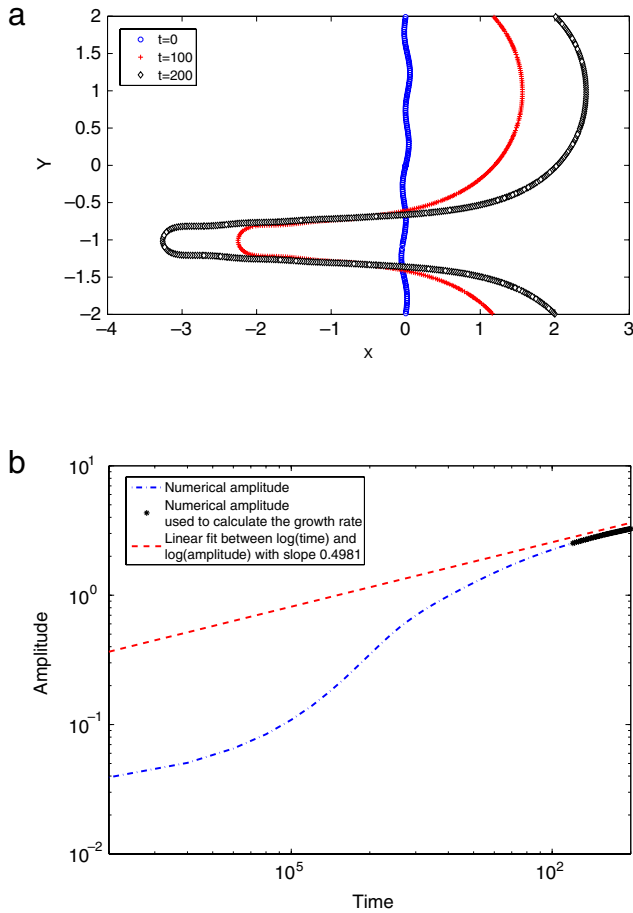


Fig. 14. Time evolution of meandering in the long wavelength regime. More specifically, the most unstable wavelength is 4 times the inter-step distance. In (a), the 0.5 contour lines of the ϕ (step position) are shown at three different times and we observe the endless growth of the amplitude. In (b), the position of the interface is plotted versus time in log–log scale. In the last stage (indicating by black stars), the fitted growth rate is $t^{0.4981}$ and this rate matches with the prediction made based on the local amplitude equation in [40,49,42] which predicts the growth rate to be $t^{0.5}$. The parameters are $\delta = 0.03$, $\rho^* = 1.0$, $\xi_- = 0.1$, $\xi_+ = 1.0$, $\beta = 0$, $\Lambda = 0.624782$, $L = 1$, domain $[-0.5, 0.5] \times [-2, 2]$, $\epsilon = 0.03$, $\Delta t = 2 \times 10^{-4}$ and $h_{\min} = 3.90625 \times 10^{-3}$.

1 (similar to the curve shown in Fig. 15, but the domain in y-direction is 4 times longer here). On the contrary, the amplitude of $\lambda_2 = 4$ will keep growing, and the amplitude is plotted in Fig. 17(b) by a black curve with dots. Note that the most unstable wavelength $\lambda_m = 1$ in this simulation. Comparing the blue curve with the black one, one notices that the growth of $\lambda_1 = 1$ dominates the growth of step initially as predicted by the linear theory. An example of the interface is shown in the inset at $t = 0.8$, and clearly $\lambda = 1$ dominates the growth. However, at later times (for example, at $t = 2.6$), $\lambda_2 = 4$ starts to dominate the growth by maintaining a moderate growth rate. This turning point is where the whole process of coarsening starts. Another example of the interface is shown in the second inset at $t = 4$. Observe that the second forward meander (counted from below) is about to disappear, and the first and second backward meanders are going to join together. This will eventually lead to a configuration at $t = 8$ as shown in Fig. 17(a). Since the growth of $\lambda_2 = 4$ tends to dominate at later times, and the domain length in y-direction equals 4, we expect only one backward meander left at the last stage. We remark that this regime is different from the long wavelength regime investigated in [39] in which they did not observe coarsening

for isotropic edge energies. We also did not find coarsening in the long wavelength regime (i.e., $\lambda_m > L$). This is because the growth of some λ_m (for example, $\lambda_m = 4$, as shown in Fig. 14) will not only dominate the growth initially (according to the linear stability theory), but also dominate the growth at later times (following the linear amplitude equation). However, in the short wavelength regime (i.e., $\lambda_m \leq L$), for example, as shown in Fig. 15, the amplitude stops growing at later times, while amplitude of $\lambda > \lambda_m$ keeps growing and dominates, leads to coarsening, and dominates the morphology eventually.

To make the coarsening clearer, we perform the following comparison experiments. On a domain of size $[-0.5, 0.5] \times [-8, 8]$, we simulate the growth of a perturbed sinusoidal curve with 5 wavelengths: $\lambda = 1, 2, 4, 8$, and 16. In case I, parameters are selected such that $\lambda_m = 4$, cf. Fig. 18(a), and coarsening does not happen in this case. In case II, however, parameters are chosen such that $\lambda_m = 1$, cf. Fig. 18(b), and coarsening does happen in this case. To see the process of coarsening clearly, trajectories of backward meander and forward meander positions obtained by numerical simulation are plotted in Fig. 18, in which a forward meander is plotted by a plus sign, and a backward meander is plotted by a star. We observe from case I that (i) the amplitude of $\lambda = 1$ and 2 does not grow at all and disappears right away, and this is because $\lambda_m = 4 > \lambda = 1, 2$; (ii) $\lambda = \lambda_m = 4$ dominates the morphology at later times. However, in case II, (i) the amplitude of $\lambda = 1$ and 2 does grow initially, and this is because that $\lambda_m = 1 \leq \lambda = 1, 2$; (ii) coarsening starts to happen around $t = 3.2$, where backward meanders (two trajectories of stars) start to join with forward meanders (one trajectory of pluses) and form new backward meanders (one trajectory of stars); (iii) this process continues until only 4 pairs of backward meanders and forward meanders left. We remark that the final morphology of case II is similar to that of the case I.

6. Conclusions

In this paper, we have presented a new phase-field model including the combined effects of edge diffusion, the Ehrlich–Schwoebel barrier and desorption to simulate epitaxial growth. A new free energy function together with a correction to the initial phase variable profile was given to efficiently capture the morphological evolution when a large deposition flux is imposed for island dynamics. A formal matched asymptotic analysis was given in the appendix to show that the phase-field model converges to the classical BCF model when the interfacial thickness vanishes. The phase-field model was then used to simulate the growth of islands and perturbed step trains. We observed that the island radius is well predicted by linear theory and that linear theory over-predicts the growth of the perturbation. Edge diffusion has also been investigated together with the Ehrlich–Schwoebel barrier. We conclude that the new phase-field model provides accurate solution to simulate the effect of edge diffusion. We also simulated the growth of a perturbed island under a variable deposition flux to demonstrate in the nonlinear regime the idea of shape control proposed by Hu et al. [29] based on linear stability theory.

Moreover, to demonstrate the versatility of the proposed phase-field model, we also investigated the linear and nonlinear regimes for step trains concentrating on the step meandering instability. We observed similar nonlinear behavior as Haußer & Voigt [39] when the meander wavelength is large compared to the terrace width. However, we found coarsening could occur when the meander wavelength is comparable to the terrace width.

In the future, since stress can play a critical role in island dynamics and step flow, we plan to investigate the effects of the elastic interactions. Recently, Haußer & Voigt [51] proposed a new

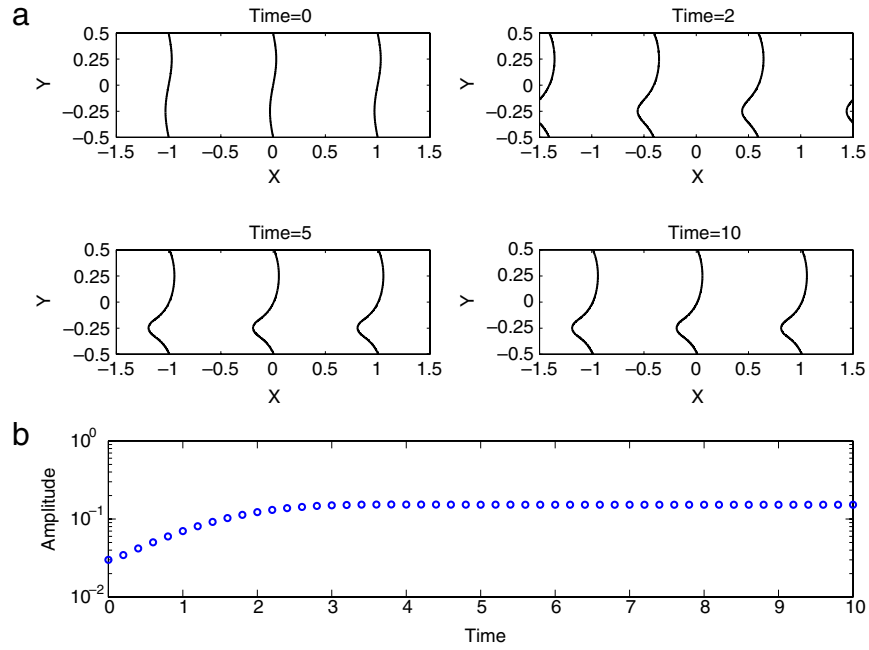


Fig. 15. The evolution of meandering in the short wavelength regime with $\lambda_m = 1$ and $\lambda_m/L = 1$. Note that 3 periods are shown in x-direction, and the step is moving from left to right. (a) The 0.5 contour lines of the step at different times demonstrate the existence of a steady-state. (b) The amplitude the interface is plotted versus time in log-linear scale. It is clear that the steps evolve to a steady shape and spacing. The parameters are $\delta = 0.003$, $\rho^* = 1.0$, $\xi_- = 0.1$, $\xi_+ = 1.0$, $\beta = 0$, $\Lambda = 0.798917$, $L = 1$, domain $[-0.5, 0.5] \times [-0.5, 0.5]$, $\epsilon = 0.015$, $\Delta t = 2 \times 10^{-4}$ and $h_{min} = 1.953125 \times 10^{-3}$.

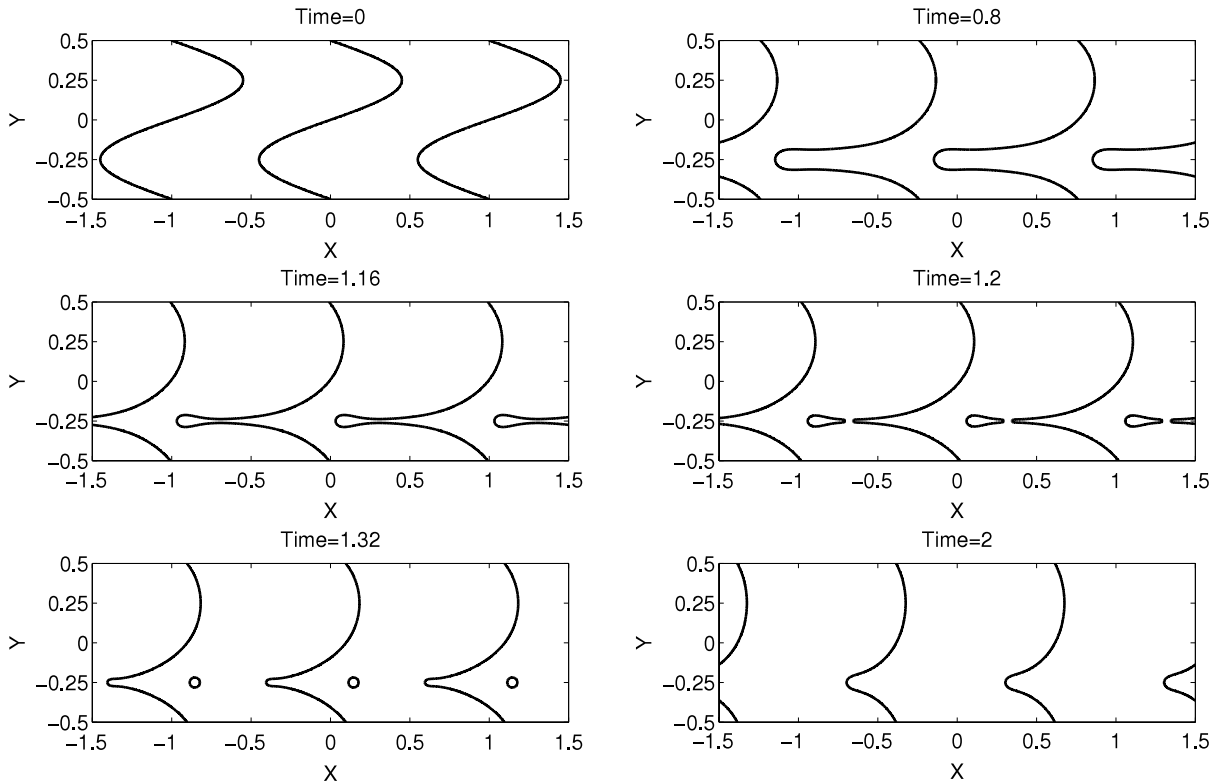


Fig. 16. Time evolution of meandering in the short wavelength regime. Note that 3 periods are shown in the x-direction, and the step is moving from left to right. (a) The 0.5 contour lines of the step at different times demonstrate the mushroom formation, pinch off, formation of vacancy island, filling of vacancy island and stabilization of amplitude. The parameters are $\delta = 0.003$, $\rho^* = 1.0$, $\xi_- = 0.1$, $\xi_+ = 1.0$, $\beta = 0$, $\Lambda = 0.798917$, $L = 1$, domain $[-0.5, 0.5] \times [-0.5, 0.5]$, $\epsilon = 0.015$, $\Delta t = 2 \times 10^{-4}$ and $h_{min} = 1.953125 \times 10^{-3}$.

sharp-interface model by extending the BCF model to incorporate coupling among the evolving steps, the transport of atoms on the terraces and along the step edges, bulk atomic diffusion and elasticity. This model should provide a basis from which a phase-

field model may be developed. We can then compare nonlinear simulations with the linear stability theory presented in [52] in which a linear stability analysis for step meandering instability with elastic interactions was studied.

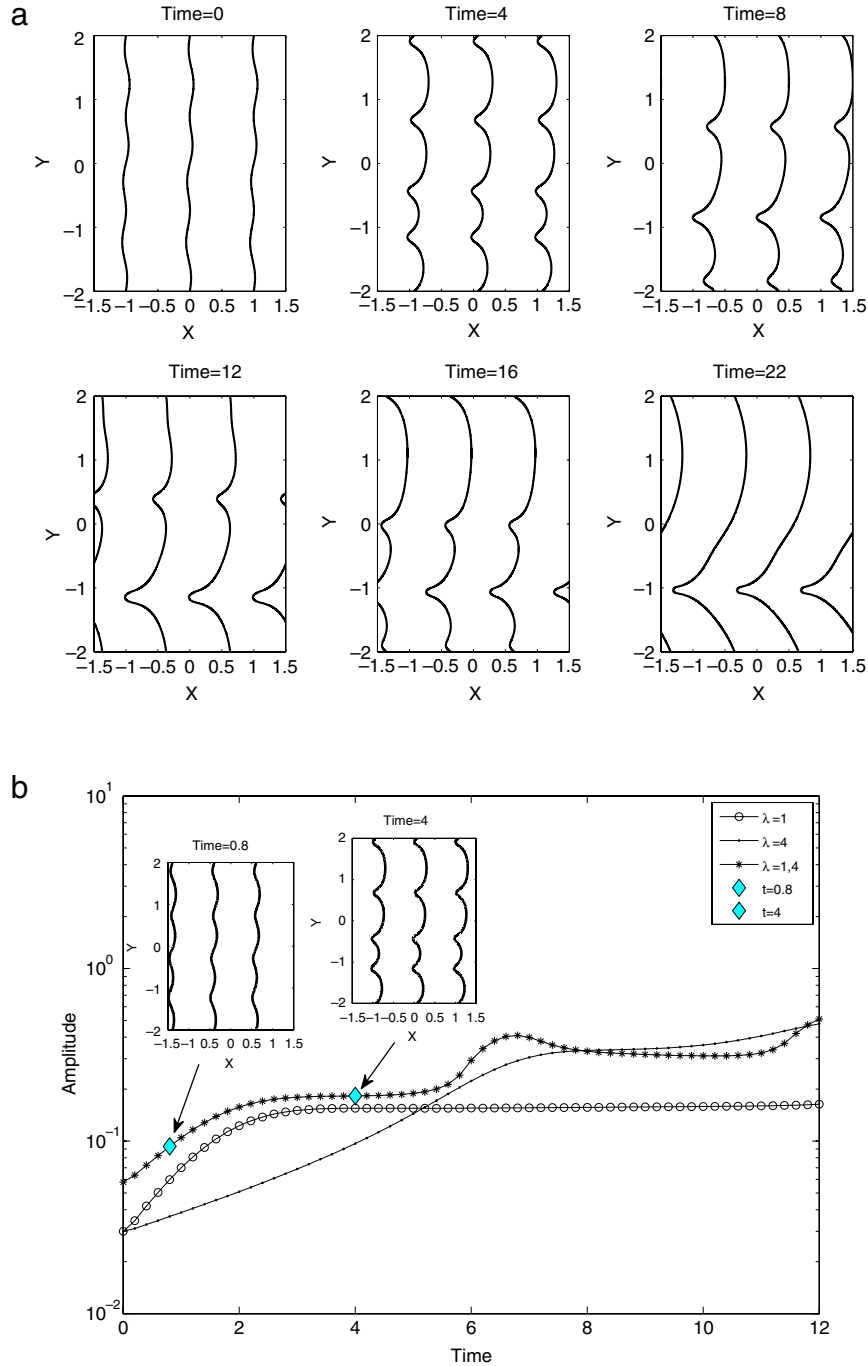


Fig. 17. Time evolution of meandering in the short wavelength regime. Note that 3 periods are showing in x -direction, and the step is moving from left to right. (a) The 0.5 contour lines of the step at different times demonstrate the existence of coarsening. (b) The amplitude of the interface is plotted versus time in semi-log scale. The parameters are $\delta = 0.003$, $\rho^* = 1.0$, $\xi_- = 0.1$, $\xi_+ = 1.0$, $\beta = 0$, $\Lambda = 0.798917$, $L = 1$, domain $[-0.5, 0.5] \times [-2, 2]$, $\epsilon = 0.015$, $\Delta t = 2 \times 10^{-4}$ and $h_{min} = 1.953125 \times 10^{-3}$.

Acknowledgments

The authors thank Shuwang Li for the fruitful discussions. J.L. and S.M. gratefully acknowledge partial support from the National Science Foundation Division of Mathematical Sciences (DMS) and the Division of Materials Research (DMR). Z.H. was also partially supported by a Doctoral Dissertation Fellowship from the Graduate School at the University of California, Irvine. A.V. acknowledges support from the 6th Framework program of EU STRP 016447 and German Science Foundation within the Collaborative Research Program SFB 609 and Grant DFG Vo899/6-2.

Appendix A. Matched asymptotic expansion

By extending the analysis in [31], we provide a matched asymptotic analysis to show the formal convergence of Eqs. (13)–(14) to Eqs. (6)–(12) as the interfacial thickness $\epsilon \rightarrow 0$.

A.1. Preliminaries

We first introduce an orthogonal curvilinear coordinate system (\tilde{r}_i, s_i) in a neighborhood of the interface $\Gamma_i(\epsilon)$, i.e., $\tilde{r}_i = \tilde{r}_i(x, y, t; \epsilon) :=$ the signed distance of (x, y) from $\Gamma_i(\epsilon)$, such that

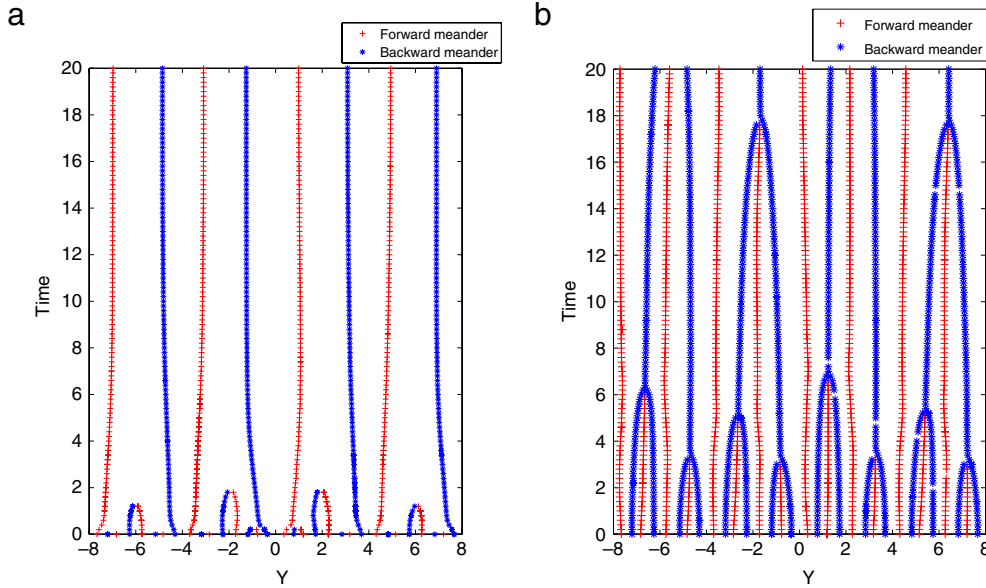


Fig. 18. Trajectories of backward meander and forward meander positions are plotted versus time. (a) $\delta = 0.03$, $\Lambda = 0.62478$, and $\epsilon = 0.03$. (b) $\delta = 0.003$, $\Lambda = 0.798917$, and $\epsilon = 0.015$. The parameters are $\rho^* = 1.0$, $\xi_- = 0.1$, $\xi_+ = 1.0$, $\beta = 0$, $L = 1$, domain $[-0.5, 0.5] \times [-8, 8]$, $\Delta t = 2 \times 10^{-4}$ and $h_{min} = 1.953125 \times 10^{-3}$.

$\tilde{r}_i > 0 \in \Omega_{i-1}$ and $\tilde{r}_i < 0 \in \Omega_i$ for $i = 1, \dots, N$; $s_i = s_i(x, y, t; \epsilon) :=$ the arc length along $\Gamma_i(\epsilon)$ to the projection of (x, y) onto $\Gamma_i(t)$. Variables ω and ϕ in Eqs. (13)–(14) are transformed to the new coordinate system:

$$\omega(x, y, t; \epsilon) = \tilde{\omega}(\tilde{r}_i, s_i, t; \epsilon),$$

$$\phi(x, y, t; \epsilon) = \tilde{\phi}(\tilde{r}_i, s_i, t; \epsilon).$$

Introducing a stretched variable $z_i := \frac{\tilde{r}_i}{\epsilon}$ for $i = 1, \dots, N$, we define

$$P(z_i, s_i, t; \epsilon) := \tilde{\omega}(\tilde{r}_i, s_i, t; \epsilon),$$

$$\Phi(z_i, s_i, t; \epsilon) := \tilde{\phi}(\tilde{r}_i, s_i, t; \epsilon).$$

In addition, the following Taylor expansion approximations for small ϵ are assumed to be valid in three regions around each interface $\Gamma_i(\epsilon)$:

(i) Away from $\Gamma_i(\epsilon)$

$$\omega(x, y, t; \epsilon) = \omega_0(x, y, t) + \epsilon \omega_1(x, y, t) + \dots, \quad (\text{A.1})$$

$$\phi(x, y, t; \epsilon) = \phi_0(x, y, t) + \epsilon \phi_1(x, y, t) + \dots, \quad (\text{A.2})$$

(ii) Matching region (overlapping domain)

$$\tilde{\omega}(\tilde{r}_i, s_i, t; \epsilon) = \tilde{\omega}_0(\tilde{r}_i, s_i, t) + \epsilon \tilde{\omega}_1(\tilde{r}_i, s_i, t) + \dots, \quad (\text{A.3})$$

$$\tilde{\phi}(\tilde{r}_i, s_i, t; \epsilon) = \tilde{\phi}_0(\tilde{r}_i, s_i, t) + \epsilon \tilde{\phi}_1(\tilde{r}_i, s_i, t) + \dots, \quad (\text{A.4})$$

(iii) Inner region near $\Gamma_i(\epsilon)$

$$P(z_i, s_i, t; \epsilon) = P_0(z_i, s_i, t) + \epsilon P_1(z_i, s_i, t) + \dots, \quad (\text{A.5})$$

$$\Phi(z_i, s_i, t; \epsilon) = \Phi_0(z_i, s_i, t) + \epsilon \Phi_1(z_i, s_i, t) + \dots, \quad (\text{A.6})$$

Eqs. (A.1)–(A.4) are called outer expansions while Eqs. (A.5)–(A.6) are called inner expansions. We assume that these expansions hold simultaneously in some overlapping region and represent the same functions, so the following matching conditions hold:

$$\lim_{\tilde{r}_i \rightarrow \pm\infty} \tilde{\omega}_0(\tilde{r}_i, s_i, t) = \lim_{z_i \rightarrow \pm\infty} P_0(z_i, s_i, t), \quad i = 1, \dots, N,$$

$$\lim_{\tilde{r}_i \rightarrow \pm\infty} \partial_{\tilde{r}_i} \tilde{\omega}_0(\tilde{r}_i, s_i, t; \epsilon) = \lim_{z_i \rightarrow \pm\infty} \partial_{z_i} P_1(z_i, s_i, t), \quad i = 1, \dots, N,$$

$$\lim_{\tilde{r}_i \rightarrow \pm\infty} \tilde{\phi}_0(\tilde{r}_i, s_i, t) = \lim_{z_i \rightarrow \pm\infty} \Phi_0(z_i, s_i, t), \quad i = 1, \dots, N,$$

$$\lim_{\tilde{r}_i \rightarrow \pm\infty} \partial_{\tilde{r}_i} \tilde{\phi}_0(\tilde{r}_i, s_i, t) = \lim_{z_i \rightarrow \pm\infty} \partial_{z_i} \Phi_1(z_i, s_i, t), \quad i = 1, \dots, N.$$

Here the functions $\omega_j, \tilde{\omega}_j, P_j, \phi_j, \tilde{\phi}_j, \Phi_j, j = 0, 1, 2, \dots$, need not to be smooth for $\tilde{r}_i = 0$. Only the existence of the one-sided limits at $\tilde{r}_i = 0$ is required. In the new coordinates (\tilde{r}_i, s_i) , the time derivative, gradient and the Laplacian operators take the following forms:

$$\partial_t = \partial_t + \partial_t \tilde{r}_i \partial_{\tilde{r}_i} + \partial_t s_i \partial_{s_i}$$

$$\nabla = \nabla_{\tilde{r}_i} \partial_{\tilde{r}_i} + \nabla_{s_i} \partial_{s_i}$$

$$\Delta = \partial_{\tilde{r}_i}^2 + |\nabla_{s_i}|^2 \partial_{s_i}^2 + \Delta \tilde{r}_i \partial_{\tilde{r}_i} + \Delta s_i \partial_{s_i}.$$

Let $\mathbf{n}_i = \mathbf{n}_i(s_i, t; \epsilon)$, $v_i = v_i(s_i, t; \epsilon)$ and $\kappa_i = \kappa(s_i, t; \epsilon)$ denote the normal, the normal velocity and the curvature, in which the normal is pointing from the upper terrace to the lower terrace. Noting that $\partial_t \tilde{r}_i = -v_i$ and $\Delta \tilde{r}_i = \kappa_i$, for $i = 1, \dots, N$, we find the time derivative, gradient and the Laplacian operators in the stretched coordinates (z_i, s_i) :

$$\partial_t = \partial_t - \frac{1}{\epsilon} v_i \partial_{z_i} + \partial_t s_i \partial_{s_i}$$

$$\nabla = \frac{1}{\epsilon} \nabla_{z_i} \partial_{z_i} + \nabla_{s_i} \partial_{s_i}$$

$$\Delta = \frac{1}{\epsilon^2} \partial_{z_i}^2 + |\nabla_{s_i}|^2 \partial_{s_i}^2 + \frac{1}{\epsilon} \kappa_i \partial_{z_i} + \Delta s_i \partial_{s_i}.$$

A.2. Outer approximation

Inserting the outer expansions Eqs. (A.1)–(A.4) into Eqs. (13)–(14) and gathering the leading order coefficients of ϵ , we get $O(1)$:

$$\partial_t \phi_0 - \beta \kappa_{ss} |\nabla \phi_0| = \nabla \cdot (M(\phi_0, \cdot) \nabla (\omega_0 + K(\phi_0, r, \cdot))) + \Lambda - \mu^2 (\omega_0 + K(\phi_0, r, \cdot) + \rho^*), \quad (\text{A.7})$$

$$0 = -G'(\phi_0). \quad (\text{A.8})$$

Eq. (A.8) has 3 solutions around each $\Gamma_i(\epsilon)$, but only two of them satisfy the initial conditions and they are $\phi_0 = i - 1$ and $\phi_0 = i$ for

$\Gamma_i(\epsilon), i = 1, \dots, N$. It then follows that $M(\phi_0, \epsilon) = 1$ for all $\epsilon > 0$. Now combining this with Eq. (A.7), we obtain the sharp interface governing equations Eqs. (6)–(7)

$$\begin{aligned} -\Delta\omega_{0,i} &= \Lambda - \mu^2(\omega_{0,i} + \rho^*) \quad \text{in } \Omega_i, \\ -\Delta\omega_{0,0} &= \Lambda - \mu^2(\omega_{0,0} + \rho^*) + \Psi \left(\frac{1}{r} - \mu^2 r \right) \quad \text{in } \Omega_0, \end{aligned}$$

for $i = 1, \dots, N$ as desired.

A.3. Taylor expansion of the mobility $M(\phi, \epsilon)$

Based on the definition of the mobility $M(\phi, \epsilon)$, we adopt the following Taylor expansion for $M(\phi, \epsilon)$ at the inner region:

$$M(\Phi(\epsilon), \epsilon) = \epsilon \frac{1}{\zeta(\Phi_0)} - \epsilon^2 \left(\frac{\zeta'(\Phi_0)\Phi_1}{\zeta(\Phi_0)^2} + \frac{1}{\zeta(\Phi_0)^2} \right) + O(\epsilon^3). \quad (\text{A.9})$$

A.4. Taylor expansion of $\nabla_s \cdot (\beta \nabla_s \kappa) | \nabla \phi |$

Recall that in the phase-field formulation, the normal \mathbf{n} can be evaluated through $\mathbf{n} = -\frac{\nabla \phi}{|\nabla \phi|}$, and the surface gradient $\nabla_s = \nabla - (\hat{\mathbf{n}} \otimes \hat{\mathbf{n}}) \nabla = \nabla - \hat{\mathbf{n}}(\hat{\mathbf{n}} \cdot \nabla)$. It follows that in the curvilinear coordinate system (z_i, s_i) , one has

$$\nabla_{s_i} = (1 - \epsilon z_i \kappa_i) s_i \partial_{s_i}.$$

Letting the curvature κ be $\kappa = -\nabla \cdot \mathbf{n}$ and setting β to be constant, it follows that

$$\nabla_{s_i} \cdot (\beta \nabla_{s_i} \kappa_i) = \beta \nabla_{s_i} \cdot \nabla_{s_i} \kappa_i = \beta \left(\partial_{s_i s_i} \kappa_i + \epsilon \kappa_i^{(1)} + O(\epsilon^2) \right),$$

where

$$\kappa_i^{(1)} = \partial_{s_i s_i s_i} \left(\frac{\partial_{s_i} \phi}{\partial_{z_i} \phi} \right) - \frac{1}{2} \partial_{s_i s_i} \partial_{z_i} \left(\frac{\partial_{s_i} \phi}{\partial_{z_i} \phi} \right)^2 - 2z_i \kappa_i \partial_{s_i s_i} \kappa_i - z_i \kappa_i^2.$$

Therefore,

$$\begin{aligned} \nabla_{s_i} \cdot (\beta \nabla_{s_i} \kappa_i) | \nabla \phi | &= \beta \left(\frac{1}{\epsilon} \partial_{s_i s_i} \kappa_i | \partial_{z_i} \phi_0 | \right. \\ &\quad \left. + \kappa_i^{(1)} | \partial_{z_i} \phi_0 | + \partial_{s_i s_i} \kappa_i | \partial_{z_i} \phi_1 | + O(\epsilon) \right). \end{aligned} \quad (\text{A.10})$$

A.5. Inner approximation

Plugging the inner expansions Eqs. (A.5)–(A.6) into Eqs. (13)–(14), using Eq. (A.9) and (A.10), and dividing Eq. (14) by ϵ , one obtains the following equations at $O(\frac{1}{\epsilon})$:

$$\begin{aligned} &-v_i \partial_{z_i} \Phi_0 - \beta \partial_{s_i s_i} \kappa_i | \partial_{z_i} \Phi_0 | \\ &= \partial_{z_i} \left(\frac{1}{\zeta(\Phi_0)} \partial_{z_i} (P_0 + \Psi \Pi_{j=1}^N (1 - \Phi_0/j) R_1) \right), \end{aligned} \quad (\text{A.11})$$

$$0 = \partial_{z_i z_i} \Phi_0 - G'(\Phi_0), \quad (\text{A.12})$$

$O(1)$:

$$\begin{aligned} &\partial_t \Phi_0 + \partial_t s_i \partial_{s_i} \Phi_0 - v_i \partial_{z_i} \Phi_1 - \beta \partial_{s_i s_i} \kappa_i | \partial_{z_i} \Phi_1 | \\ &= \partial_{z_i} \left(\frac{\partial_{z_i} (P_1 + \Psi \Pi_{j=1}^N (1 - \Phi_0/j) z_i - \Psi \Phi_1 R_1)}{\zeta(\Phi_0)} \right. \\ &\quad \left. - \frac{1 + \zeta'(\Phi_0)\Phi_1}{\zeta(\Phi_0)^2} \partial_{z_i} (P_0 + \Psi \Pi_{j=1}^N (1 - \Phi_0/j) R_1) \right) \end{aligned}$$

$$\begin{aligned} &+ \kappa_i \frac{\partial_{z_i} (P_0 + \Psi \Pi_{j=1}^N (1 - \Phi_0/j) R_1)}{\zeta(\Phi_0)} \\ &+ \Lambda - \mu^2 (P_0 + \Psi \Pi_{j=1}^N (1 - \Phi_0/j) R_1 + \rho^*), \end{aligned} \quad (\text{A.13})$$

$$\begin{aligned} &-\alpha (v_i \partial_{z_i} \Phi_0 + \beta \partial_{s_i s_i} \kappa_i | \partial_{z_i} \Phi_0 |) \\ &= \kappa_i \partial_{z_i} \Phi_0 + \partial_{z_i z_i} \Phi_1 - \Phi_1 G''(\Phi_0) \\ &+ \frac{1}{\rho^* \delta} (P_0 + \Psi \Pi_{j=1}^N (1 - \Phi_0/j) R_1). \end{aligned} \quad (\text{A.14})$$

By the matching condition $\lim_{z_i \rightarrow \pm\infty} \Phi_0 = \lim_{\tilde{r}_i \rightarrow \pm 0} \tilde{\phi}_0$, and the solution to Eq. (A.8), $\phi_0 = i - 1$ in Ω_{i-1} and $\phi_0 = i$ in Ω_i , we get $\lim_{z_i \rightarrow +\infty} \Phi_0 = \lim_{\tilde{r}_i \rightarrow +0} \tilde{\phi}_0 = i - 1$ as well as $\lim_{z_i \rightarrow -\infty} \Phi_0 = \lim_{\tilde{r}_i \rightarrow -0} \tilde{\phi}_0 = i$. Now let $\psi = \psi(z_i)$ be the unique solution to the differential equation (A.12), we get

$$\begin{aligned} \psi''(z_i) - \frac{\partial G(\psi(z_i))}{\partial \psi} &= 0, \quad \psi(+\infty) = i - 1, \\ \psi(0) = i - \frac{1}{2}, \quad \psi(-\infty) &= i. \end{aligned} \quad (\text{A.15})$$

Applying a centering condition [53], one obtains from Eq. (A.15)

$$\Phi_0(z_i, s_i, t) = \psi(z_i)$$

Therefore Φ_0 only depends on z_i . Furthermore since $\lim_{z_i \rightarrow \pm\infty} \partial_{z_i} \Phi_0(z_i) = 0$ (which is a consequence of $\lim_{z_i \rightarrow \pm\infty} G'(\Phi_0) = 0$), $\lim_{z_i \rightarrow +\infty} \Phi_0 = i - 1$ and $\lim_{z_i \rightarrow -\infty} \Phi_0 = i$, it follows

$$\lim_{z_i \rightarrow \pm\infty} \partial_{z_i} \Phi_0(z_i) = 0. \quad (\text{A.16})$$

Multiplying Eq. (A.12) by $\partial_{z_i} \Phi_0$, integrating from $-\infty$ to z and using $\lim_{z_i \rightarrow +\infty} \Phi_0 = i - 1$, $\lim_{z_i \rightarrow -\infty} \Phi_0 = i$ as well as Eq. (A.16), one arrives at

$$\partial_{z_i} \Phi_0 = -\sqrt{2G(\Phi_0)}. \quad (\text{A.17})$$

By definition and the centering condition one also has

$$\Phi_0(0, s_i, t) = \Phi_0(0) = \frac{1}{2}. \quad (\text{A.18})$$

Also, according to Eq. (A.11), there exists a constant $c = c(s_i, t)$ such that

$$\begin{aligned} &\partial_{z_i} (P_0 + \Psi \Pi_{j=1}^N (1 - \Phi_0/j) R_1) \\ &= (c + (\beta \partial_{s_i s_i} \kappa_i - v_i) \Phi_0) \zeta(\Phi_0). \end{aligned} \quad (\text{A.19})$$

Substituting (A.19) into (A.13) leads to

$$\begin{aligned} &-v_i \partial_{z_i} \Phi_1 - \beta \partial_{s_i s_i} \kappa_i | \partial_{z_i} \Phi_1 | \\ &= \partial_{z_i} \left(\frac{\partial_{z_i} (P_1 + \Psi \Pi_{j=1}^N (1 - \Phi_0/j) z_i - \Psi \Phi_1 R_1)}{\zeta(\Phi_0)} \right. \\ &\quad \left. - \frac{1 + \zeta'(\Phi_0)\Phi_1}{\zeta(\Phi_0)} (c + (\beta \partial_{s_i s_i} \kappa_i - v_i) \Phi_0) \right) \\ &\quad + \kappa_i (c + (\beta \partial_{s_i s_i} \kappa_i - v_i) \Phi_0) \\ &\quad + \Lambda - \mu^2 (P_0 + \Psi \Pi_{j=1}^N (1 - \Phi_0/j) R_1 + \rho^*) \end{aligned} \quad (\text{A.20})$$

Note that by the matching condition $\lim_{z_i \rightarrow \pm\infty} \partial_{z_i} \Phi_1 = \lim_{\tilde{r}_i \rightarrow \pm 0} \tilde{\phi}_1 = 0$ and that $\lim_{z_i \rightarrow \pm\infty} \zeta(\Phi_0(z_i)) = 0$ (with $1/\zeta(\Phi_0)$ growing exponentially), one gets the following asymptotic behavior of Eq. (A.20)

$$\begin{aligned} &\lim_{z_i \rightarrow \pm\infty} (\partial_{z_i} P_1 + \Psi \Pi_{j=1}^N (1 - \Phi_0/j)) \\ &= \lim_{z_i \rightarrow \pm\infty} \{ (1 + \zeta'(\Phi_0)\Phi_1) (c + (\beta \partial_{s_i s_i} \kappa_i - v_i) \Phi_0) \} \\ &= c + (\beta \partial_{s_i s_i} \kappa_i - v_i) (1/2 \mp 1/2), \end{aligned} \quad (\text{A.21})$$

where the special form of ζ such that $\lim_{z_i \rightarrow \pm\infty} \zeta'(\Phi_0(z_i)) = 0$ and the boundedness of Φ_1 was used.

Using the matching condition $\lim_{z_i \rightarrow \pm\infty} \partial_{z_i} P_1(z_i, s_i, t) = \lim_{\tilde{r}_i \rightarrow \pm 0} \partial_{\tilde{r}_i} \tilde{\omega}_0(\tilde{r}_i, s_i, t)$ in Eq. (A.21), we get

$$\nabla \omega_{0,i} \cdot \mathbf{n}_i = c + (\beta \partial_{s_i s_i} \kappa_i - v_i), \tag{A.22}$$

$$\nabla \omega_{0,i-1} \cdot \mathbf{n}_i = c, \tag{A.23}$$

$$\nabla \omega_{0,0} \cdot \mathbf{n}_1 + \Psi = c, \tag{A.24}$$

for $i = 2, \dots, N$, which are equivalent to the sharp interface velocity Eqs. (12)–(12)

$$\begin{aligned} v_i &= -\nabla \omega_{0,i} \cdot \mathbf{n}_i + \nabla \omega_{0,i-1} \cdot \mathbf{n}_i + \nabla_{s_i} \cdot (\beta \nabla_{s_i} \kappa_i) \\ &\quad \text{on } \Gamma_i, \\ v_1 &= -\nabla \omega_{0,1} \cdot \mathbf{n}_1 + \nabla \omega_{0,0} \cdot \mathbf{n}_1 + \nabla_{s_1} \cdot (\beta \nabla_{s_1} \kappa_1) + \Psi \\ &\quad \text{on } \Gamma_1, \end{aligned}$$

for $i = 2, \dots, N$.

We now turn to use Eq. (A.14) to solve for Φ_0 . Differentiating Eq. (A.14) with respect to z and solving for $(\partial_{z_i} P_1 + \Psi \prod_{j=1}^N (1 - \Phi_0/j))$, then substituting the resultant expression into Eq. (A.19), we get

$$\begin{aligned} & -\partial_{z_i} (\alpha(v_i - \beta \partial_{s_i s_i} \kappa_i) \partial_{z_i} \Phi_0 + \partial_{z_i z_i} \Phi_1 + \kappa_i \partial_{z_i} \Phi_0 - \Phi_1 G''(\Phi_0)) \\ &= \frac{1}{\rho^* \delta} (c - (\beta \partial_{s_i s_i} \kappa_i - v_i) \Phi_0) \zeta(\Phi_0). \end{aligned} \tag{A.25}$$

Multiplying Eq. (A.25) by $\Phi_0 - (i - 1)$, and integrating along the z -axis, one gets:

$$\begin{aligned} & -\int_{-\infty}^{\infty} \partial_{z_i} (\alpha(v_i - \beta \partial_{s_i s_i} \kappa_i) \partial_{z_i} \Phi_0 + \partial_{z_i z_i} \Phi_1 \\ & \quad + \kappa_i \partial_{z_i} \Phi_0 - \Phi_1 G''(\Phi_0)) (\Phi_0 - (i - 1)) dz_i \\ &= \frac{1}{\rho^* \delta} \int_{-\infty}^{\infty} (c - (\beta \partial_{s_i s_i} \kappa_i - v_i) \Phi_0) \\ & \quad \times \zeta(\Phi_0) (\Phi_0 - (i - 1)) dz_i. \end{aligned} \tag{A.26}$$

Using Eq. (A.17), we have

$$\begin{aligned} & -\int_{-\infty}^{\infty} \partial_{z_i} ((\kappa_i + \alpha(v_i - \beta \partial_{s_i s_i} \kappa_i)) \partial_{z_i} \Phi_0) (\Phi_0 - (i - 1)) dz_i \\ &= \int_{i-1}^i (\kappa_i + \alpha(v_i - \beta \partial_{s_i s_i} \kappa_i)) \sqrt{2G(\phi)} d\phi. \end{aligned} \tag{A.27}$$

Using integration by parts and Eq. (A.16), we find

$$\begin{aligned} & -\int_{-\infty}^{\infty} \partial_{z_i} (\partial_{z_i z_i} \Phi_1 - \Phi_1 G''(\Phi_0)) (\Phi_0 - (i - 1)) dz_i \\ &= \lim_{z_i \rightarrow -\infty} \Phi_0 (\partial_{z_i z_i} \Phi_1 - \Phi_1 G''(\Phi_0)) \\ & \quad + \int_{-\infty}^{\infty} \partial_{z_i} \Phi_0 (\partial_{z_i z_i} \Phi_1 - \Phi_1 G''(\Phi_0)) dz_i. \end{aligned} \tag{A.28}$$

Eq. (A.14) and the matching condition $\lim_{z_i \rightarrow \pm\infty} P_0 = \lim_{\tilde{r}_i \rightarrow \pm 0} \tilde{\omega}_0$ imply that

$$\begin{aligned} \lim_{z_i \rightarrow -\infty} \Phi_0 (\partial_{z_i z_i} \Phi_1 - \Phi_1 G''(\Phi_0)) &= -\frac{1}{\rho^* \delta} \omega_{0,i}, \\ &\text{for } i = 1, \dots, N. \end{aligned} \tag{A.29}$$

Next, using integration by parts twice and Eq. (A.16), one gets

$$\begin{aligned} & \int_{-\infty}^{\infty} \partial_{z_i} \Phi_0 (\partial_{z_i z_i} \Phi_1 - \Phi_1 G''(\Phi_0)) dz_i \\ &= \partial_{z_i} \Phi_0 \partial_{z_i} \Phi_1 \Big|_{-\infty}^{\infty} - \Phi_1 \partial_{z_i z_i} \Phi_0 \Big|_{-\infty}^{\infty} \\ & \quad + \int_{-\infty}^{\infty} \Phi_i \partial_{z_i} (\partial_{z_i z_i} \Phi_0 - G'(\Phi_0)) dz_i \\ &= 0. \end{aligned} \tag{A.30}$$

We have evaluated all terms on the left-hand-side of Eq. (A.26). We next evaluate the right-hand-side of Eq. (A.26).

$$\begin{aligned} & \frac{1}{\rho^* \delta} \int_{-\infty}^{\infty} (c - (\beta \partial_{s_i s_i} \kappa_i - v_i) \Phi_0) \zeta(\Phi_0) (\Phi_0 - (i - 1)) dz_i \\ &= \frac{1}{\rho^* \delta} \int_{-\infty}^{\infty} (c - (\beta \partial_{s_i s_i} \kappa_i - v_i) \Phi_0) \\ & \quad \times \frac{\zeta(\Phi_0) \partial_{z_i} \Phi_0}{\partial_{z_i} \Phi_0} (\Phi_0 - (i - 1)) dz_i \\ &= \frac{1}{\rho^* \delta} \left\{ c \int_{i-1}^i \frac{\zeta(\phi)}{\sqrt{2G(\phi)}} \phi d\phi + (\beta \partial_{s_i s_i} \kappa_i - v_i) \right. \\ & \quad \left. \times \int_{i-1}^i \frac{\zeta(\phi)}{\sqrt{2G(\phi)}} \phi^2 d\phi \right\}. \end{aligned} \tag{A.31}$$

Putting Eqs. (S12-1)–(S12-5) together, we get

$$\begin{aligned} & -\omega_{0,i} + \rho^* \delta (\kappa_i + \alpha(v_i - \beta \partial_{s_i s_i} \kappa_i)) \int_{i-1}^i \sqrt{2G(\phi)} d\phi \\ &= c \int_{i-1}^i \frac{\zeta(\phi)}{\sqrt{2G(\phi)}} \phi d\phi + (\beta \partial_{s_i s_i} \kappa_i - v_i) \int_{i-1}^i \frac{\zeta(\phi)}{\sqrt{2G(\phi)}} \phi^2 d\phi, \end{aligned} \tag{A.32}$$

on Γ_i for $i = 1, \dots, N$.

Similarly, multiplying Eq. (A.25) by $i - \Phi_0$ will eventually lead to

$$\begin{aligned} & \omega_{0,i-1} - \rho^* \delta (\kappa_i + \alpha(v_i - \beta \partial_{s_i s_i} \kappa_i)) \int_{i-1}^i \sqrt{2G(\phi)} d\phi \\ &= c \int_{i-1}^i \frac{\zeta(\phi)}{\sqrt{2G(\phi)}} (i - \phi) d\phi \\ & \quad + (\beta \partial_{s_i s_i} \kappa_i - v_i) \left\{ -\int_{i-1}^i \frac{\zeta(\phi)}{\sqrt{2G(\phi)}} \phi^2 d\phi \right. \\ & \quad \left. + \int_{i-1}^i \frac{\zeta(\phi)}{\sqrt{2G(\phi)}} \phi d\phi \right\}, \end{aligned} \tag{A.33}$$

on Γ_i for $i = 2, \dots, N$ and

$$\begin{aligned} & \omega_{0,0} + \Psi R_1 - \rho^* \delta (\kappa_1 + \alpha(v_1 - \beta \partial_{s_1 s_1} \kappa_1)) \int_0^1 \sqrt{2G(\phi)} d\phi \\ &= c \int_0^1 \frac{\zeta(\phi)}{\sqrt{2G(\phi)}} (1 - \phi) d\phi \\ & \quad + (\beta \partial_{s_1 s_1} \kappa_1 - v_1) \left\{ -\int_0^1 \frac{\zeta(\phi)}{\sqrt{2G(\phi)}} \phi^2 d\phi \right. \\ & \quad \left. + \int_0^1 \frac{\zeta(\phi)}{\sqrt{2G(\phi)}} \phi d\phi \right\} \\ & \quad \text{on } \Gamma_1. \end{aligned} \tag{A.34}$$

Now we choose $G(\phi)$ such that

$$\int_{i-1}^i \sqrt{2G(\phi)} d\phi = 1, \quad \text{for } i = 1, \dots, N. \tag{A.35}$$

Then applying Eqs. (A.22)–(A.24), and (A.35) in Eqs. (A.32)–(A.34), we get

$$\begin{aligned} & -\omega_{0,i} + \rho^* \delta \kappa_i = (\nabla \omega_{0,i} \cdot \mathbf{n}_i) \int_{i-1}^i \frac{\zeta(\phi)}{\sqrt{2G(\phi)}} \phi d\phi \\ & \quad + (\beta \partial_{s_i s_i} \kappa_i - v_i) \left\{ \rho^* \delta \alpha - \int_{i-1}^i \frac{\zeta(\phi)}{\sqrt{2G(\phi)}} (i - \phi) \phi d\phi \right\} \quad \text{on } \Gamma_i, \\ & \omega_{0,i-1} - \rho^* \delta \kappa_i = (\nabla \omega_{0,i-1} \cdot \mathbf{n}_i) \int_{i-1}^i \frac{\zeta(\phi)}{\sqrt{2G(\phi)}} (i - \phi) d\phi \end{aligned}$$

$$\begin{aligned}
& + (\beta \partial_{s_i} \kappa_i - v_i) \left\{ -\rho^* \delta \alpha + \int_{i-1}^i \frac{\zeta(\phi)}{\sqrt{2G(\phi)}} (i - \phi) \phi \, d\phi \right\} \\
& \quad \text{on } \Gamma_i, \\
(\omega_{0,0} + \Psi R_1) - \rho^* \delta \kappa_1 & = (\nabla \omega_{0,0} \cdot \mathbf{n}_1 + \Psi) \\
& \times \int_0^1 \frac{\zeta(\phi)}{\sqrt{2G(\phi)}} (1 - \phi) \, d\phi \\
& + (\beta \partial_{s_1} \kappa_1 - v_1) \left\{ -\rho^* \delta \alpha + \int_0^1 \frac{\zeta(\phi)}{\sqrt{2G(\phi)}} (1 - \phi) \phi \, d\phi \right\} \\
& \quad \text{on } \Gamma_1, \\
\text{for } i & = 2, \dots, N. \\
\text{Now choosing} \\
\alpha & = \frac{1}{\rho^* \delta} \int_{i-1}^i \frac{\zeta(\phi)}{\sqrt{2G(\phi)}} (1 - \phi) \phi \, d\phi \quad \text{for } i = 1, \dots, N, \quad (\text{A.36})
\end{aligned}$$

we get

$$\begin{aligned}
-\omega_{0,i} + \rho^* \delta \kappa_i & = (\nabla \omega_{0,i} \cdot \mathbf{n}_i) \int_{i-1}^i \frac{\zeta(\phi)}{\sqrt{2G(\phi)}} \phi \, d\phi, \\
\omega_{0,i-1} - \rho^* \delta \kappa_i & = (\nabla \omega_{0,i-1} \cdot \mathbf{n}_i) \int_{i-1}^i \frac{\zeta(\phi)}{\sqrt{2G(\phi)}} (i - \phi) \, d\phi, \\
(\omega_{0,0} + \Psi R_1) - \rho^* \delta \kappa_1 \\
& = (\nabla \omega_{0,0} \cdot \mathbf{n}_1 + \Psi) \int_0^1 \frac{\zeta(\phi)}{\sqrt{2G(\phi)}} (1 - \phi) \, d\phi,
\end{aligned}$$

for $i = 2, \dots, N$.

Finally, let us define $\zeta(\phi) = \gamma \phi^p G(\phi)$, where γ and p satisfy the following equations

$$\begin{aligned}
\int_{i-1}^i \frac{\zeta(\phi)}{\sqrt{2G(\phi)}} \phi \, d\phi & = \xi_+, \\
\int_{i-1}^i \frac{\zeta(\phi)}{\sqrt{2G(\phi)}} (i - \phi) \, d\phi & = \xi_-. \quad (\text{A.37})
\end{aligned}$$

We now get the boundary conditions Eqs. (8)–(10)

$$\begin{aligned}
-\xi_+ \nabla \omega_{0,i} \cdot \mathbf{n}_i & = \omega_{0,i} - \rho^* \delta \kappa_i \quad \text{on } \Gamma_i, \\
\xi_- \nabla \omega_{0,i-1} \cdot \mathbf{n}_i & = \omega_{0,i-1} - \rho^* \delta \kappa_i \quad \text{on } \Gamma_i, \\
\xi_- \nabla \omega_{0,0} \cdot \mathbf{n}_1 & = \omega_{0,0} - \rho^* \delta \kappa_1 + \Psi (R_1 - \xi_-) \quad \text{on } \Gamma_1, \\
\text{for } i & = 2, \dots, N.
\end{aligned}$$

Appendix B. Numerical calculation of the surface Laplacian of the curvature

In this section, we outline the computation of the surface Laplacian of the curvature. We start with the calculation for the normal vectors at a cell vertex, which is done by differentiating the phase variable in the four surrounding cells [54]. For example, the normal vector at the top right vertex of a cell centered at (i, j) is given by

$$\begin{aligned}
\mathbf{n}_{i+\frac{1}{2}, j+\frac{1}{2}} & = \left(n_{i+\frac{1}{2}, j+\frac{1}{2}}^x, n_{i+\frac{1}{2}, j+\frac{1}{2}}^y \right) \\
& = \left(\frac{\phi_{i+\frac{1}{2}, j+\frac{1}{2}}^x}{\sqrt{(\phi_{i+\frac{1}{2}, j+\frac{1}{2}}^x)^2 + (\phi_{i+\frac{1}{2}, j+\frac{1}{2}}^y)^2 + 10^{-8}}}, \right. \\
& \quad \left. \frac{\phi_{i+\frac{1}{2}, j+\frac{1}{2}}^y}{\sqrt{(\phi_{i+\frac{1}{2}, j+\frac{1}{2}}^x)^2 + (\phi_{i+\frac{1}{2}, j+\frac{1}{2}}^y)^2 + 10^{-8}}} \right),
\end{aligned}$$

in which

$$\begin{aligned}
\phi_{i+\frac{1}{2}, j+\frac{1}{2}}^x & = \frac{\phi_{i+1, j} - \phi_{i, j} + \phi_{i+1, j+1} - \phi_{i, j+1}}{2\Delta x}, \\
\phi_{i+\frac{1}{2}, j+\frac{1}{2}}^y & = \frac{\phi_{i, j+1} - \phi_{i, j} + \phi_{i+1, j+1} - \phi_{i+1, j}}{2\Delta y}.
\end{aligned}$$

The curvature is calculated at cell centers from the four vertex-centered normals that closest to the cell center [54]:

$$\begin{aligned}
\kappa_{i, j} & = \frac{1}{2\Delta x} \left(n_{i+\frac{1}{2}, j+\frac{1}{2}}^x - n_{i-\frac{1}{2}, j+\frac{1}{2}}^x + n_{i+\frac{1}{2}, j-\frac{1}{2}}^x - n_{i-\frac{1}{2}, j-\frac{1}{2}}^x \right) \\
& \quad + \frac{1}{2\Delta y} \left(n_{i+\frac{1}{2}, j+\frac{1}{2}}^y - n_{i+\frac{1}{2}, j-\frac{1}{2}}^y + n_{i-\frac{1}{2}, j+\frac{1}{2}}^y - n_{i-\frac{1}{2}, j-\frac{1}{2}}^y \right).
\end{aligned}$$

To calculate the surface Laplacian, we follow Xu and Zhao [55] and write

$$\nabla_s \cdot \nabla_s = \Delta - \frac{\partial^2}{\partial \mathbf{n}^2} - \kappa \frac{\partial}{\partial \mathbf{n}} = \Delta - \mathbf{n} D^2 \mathbf{n} - \kappa \mathbf{n} \cdot \nabla,$$

in which D^2 is the Hessian of the applied function. Finally, $|\nabla \phi_{i, j}^k|$ is obtained at the cell center:

$$|\nabla \phi_{i, j}| = \frac{1}{2} \sqrt{\left(\frac{\phi_{i+1, j} - \phi_{i-1, j}}{\Delta x} \right)^2 + \left(\frac{\phi_{i, j+1} - \phi_{i, j-1}}{\Delta y} \right)^2}.$$

Since we are dealing with a phase-field function, a cut-off function is needed to ensure the calculation only applies around the interface. A typical choice of such function is

$$f(\phi) = \begin{cases} 1, & \text{if } \phi \in [0.4, 0.6], \\ 0, & \text{otherwise.} \end{cases}$$

Therefore, the actual term appears in the numerical scheme is $f(\phi) \nabla_s \cdot (\beta \nabla_{s, \kappa}) |\nabla \phi|$ instead of $\nabla_s \cdot (\beta \nabla_{s, \kappa}) |\nabla \phi|$ in Eqs. (13) and (14). Putting this form back into the asymptotic analysis, one finds that the effective edge diffusion is scaled by $\int_0^1 f(\phi) d\phi = 0.2$, for the function used above.

Appendix C. The phase-field initial condition

We outline the phase-field initial condition used in island dynamic simulations. Let us first define the distance from any point (x, y) in the domain to the center of the island to be $r(x, y)$, and define the island boundary by $R(x, y; \ell) = R(0)(1 + P(0) \cos(\ell \theta(x, y)))$, where $R(0)$ and $P(0)$ are initial radius and shape factor. Here ℓ is the wavenumber, and $\theta(x, y)$ is the angle between the tangent at (x, y) and x -axis. As mentioned in Section 5.1.1, the initial condition for the phase variable $\phi(x, y)$ at (x, y) is

$$\phi(x, y) = \phi(r(x, y)) = \phi_0(r(x, y)) + \epsilon \phi_1(r(x, y)), \quad (\text{C.1})$$

where

$$\phi_0(r(x, y)) = \frac{1}{2} \left[1 - \tanh \left(\frac{r(x, y) - R(x, y; \ell)}{0.1 \sqrt{2/b\epsilon}} \right) \right],$$

$$\phi_1(r(x, y)) = \frac{\omega_{\text{linear}}}{\rho^* \delta G''(\phi_0(r(x, y)))}.$$

Here the parameter b is define in Eq. (15) and ω_{linear} following from the linear stability analysis by Hu et al. [29] is

(i) If $0 \leq r(x, y) < R(x, y; \ell)$, then

$$\begin{aligned}
\omega_{\text{linear}} & = -\frac{\Lambda}{4} r^2(x, y) + \frac{\rho^* (R(0) + \delta)}{R(0)} + \frac{\Lambda R(0) (R(0) + 2\xi_+)}{4} \\
& \quad + \frac{2\delta \rho^* (\ell^2 - 1) + \Lambda (R(0))^2 (R(0) + \xi_+)}{2(R(0))^{\ell+1} (R(0) + \ell\xi_+)} \\
& \quad \times (R(x, y; \ell) - R(0)) r^\ell(x, y)
\end{aligned}$$

(ii) If $R(x, y; \ell) \leq r(x, y) < 1$, then we obtain the equation as given in Box I.

$$\omega_{\text{linear}} = -\frac{\Lambda}{4}r^2(x, y) + \frac{\Lambda}{2}\ln(r(x, y)) + \frac{4\rho^*(\delta + R(0)) + \Lambda((R(0))^3 + 2\xi_- - 2(R(0))^2\xi_-) - 2\Lambda R(0)\ln(R(0))}{4R(0)} + C(R(x, y; \ell) - R(0))(r^\ell(x, y) + r^{-\ell}(x, y)),$$

where

$$C = \frac{(R(0))^{\ell-1}(2\delta\rho^*(\ell^2 - 1) - \Lambda(R(0) - (R(0))^3 + \xi_- + (R(0))^2\xi_-)) + 2\Psi(R(0) + \xi_-)}{2(R(0) + (R(0))^2\ell(R(0) - \ell\xi_-) + \ell\xi_-)}.$$

Box I

Appendix D. Dispersion relation of step trains

Let L be the inter-terrace distance between steps, and $\omega(\ell)$ be the growth rate of the amplitude of wave number ℓ . Following the analysis is [10], one finds

$$\omega(\ell) = -f_1(\ell, L, \xi_-, \xi_+, \delta, \rho^*) - (\xi_- - \xi_+) \Lambda f_2(\ell, L, \xi_-, \xi_+) - f_3(\ell, \beta), \quad (\text{D.1})$$

for the case without desorption. Here

$$\begin{aligned} f_1(\ell, L, \xi_-, \xi_+, \delta, \rho^*) &= \frac{\delta\ell^3\rho^*(-2 + 2\cosh(\ell L) + \ell(\xi_- + \xi_+)\sinh(\ell L))}{\ell(\xi_- + \xi_+)\cosh(\ell L) + (1 + \ell^2\xi_-\xi_+)\sinh(\ell L)} \\ f_2(\ell, L, \xi_-, \xi_+) &= \frac{\ell\sinh(\frac{\ell L}{2})(\ell L(L + 2(\xi_- + \xi_+))\cosh(\frac{\ell L}{2}) - 2(\xi_- + \xi_+)\sinh(\frac{\ell L}{2}))}{(L + \xi_- + \xi_+)(\ell(\xi_- + \xi_+)\cosh(\ell L) + (1 + \ell^2\xi_-\xi_+)\sinh(\ell L))} \\ f_3(\ell, \beta) &= \beta\ell^4. \end{aligned}$$

Using $\cosh(x) \geq 1$ for $x \geq 1$, we note f_1 is positive definite. f_2 is also positive definite though not obvious and f_3 is positive definite. Therefore, if $\xi_- > \xi_+$ (i.e., $k_- < k_+$), the growth of step trains is always stable. Conversely, if $\xi_- < \xi_+$ (i.e., $k_- > k_+$), morphologically unstable growth may occur.

Appendix E. Supplementary data

Supplementary material related to this article can be found online at doi:10.1016/j.physd.2011.09.004.

References

- [1] J. Krug, Introduction to step dynamics and step instabilities, in: A. Voigt (Ed.), Multiscale Modeling in Epitaxial Growth, Birkhäuser, 2005, pp. 69–96.
- [2] A. Voigt, Multiscale Modeling in Epitaxial Growth, Birkhäuser, Berlin, 2005.
- [3] X.L. Wang, V. Voliotis, Epitaxial growth and optical properties of semiconductor quantum wires, J. Appl. Phys. 99 (2006) 121301.
- [4] H.E. Katz, Recent advances in semiconductor performance and printing processes for organic transistor-based electronics, Chem. Mater. 16 (2004) 4748.
- [5] K.A. Fichtorn, M.L. Merrick, M. Scheffler, Nanostructures at surfaces from substrate-mediated interactions, Phys. Rev. B 68 (2003) 041404.
- [6] P. Zoontjens, T.P. Schulze, S.C. Hendy, Hybrid method for modeling epitaxial growth: Kinetic Monte Carlo plus molecular dynamics, Phys. Rev. B 76 (2007) 245418.
- [7] M. Rusanen, I.T. Koponen, J. Heinonen, T. Ala-Nissilä, Instability and wavelength selection during step flow growth of metal surfaces vicinal to fcc(001), Phys. Rev. Lett. 86 (2001) 5317–5320.
- [8] F. Much, M. Ahr, M. Biehl, W. Kinzel, A kinetic Monte Carlo method for the simulation of heteroepitaxial growth, Comput. Phys. Comm. 147 (2002) 226–229.
- [9] G. Russo, P. Smereka, Computation of strained epitaxial growth in three dimensions by kinetic Monte Carlo, J. Comput. Phys. 214 (2006) 809–828.
- [10] G.S. Bales, A. Zangwill, Morphological instability of a terrace edge during step-flow growth, Phys. Rev. B 41 (1990) 5500.
- [11] R.E. Caflisch, W. E., M.F. Gyure, B. Merriman, C. Ratsch, Kinetic model for a step edge in epitaxial growth, Phys. Rev. E 59 (1999) 6879.
- [12] R.E. Caflisch, B. Li, Analysis of island dynamics in epitaxial growth of thin films, Multiscale Model. Simul. 1 (2003) 150.
- [13] M. Avignon, B.K. Chakraverty, Morphological stability of two-dimensional nucleus, Roy. Soc. Lond. 310 (1969) 277.
- [14] W.W. Mullins, R.F. Sekerka, Morphological stability of a particle growing by diffusion or heat flow, J. Appl. Phys. 34 (1963) 323.
- [15] B. Li, A. Rätz, A. Voigt, Stability of a circular epitaxial island, Physica D 198 (2004) 231.
- [16] R.J. Asaro, W.A. Tiller, Interface morphology development during stress corrosion cracking: part I. via surface diffusion, Metall. Trans. 3 (1972) 1789.
- [17] M. Grinfeld, Instability of the separation boundary between a non-hydrostatically stressed elastic body and a melt, Dokl. Akad. Nauk SSSR 290 (1986) 1358; Sov. Phys. Dokl. 31 (10) (1987) 831.
- [18] Nozières, On the motion of steps on a vicinal surface, J. Phys. France 48 (1987) 1605.
- [19] N. Israeli, D. Kandel, Profile scaling in decay of nanostructure, Phys. Rev. Lett. 80 (1998) 3300.
- [20] N. Israeli, D. Kandel, Profile of a decaying crystalline cone, Phys. Rev. B 60 (1999) 5946.
- [21] N. Israeli, D. Kandel, Decay of one-dimensional surface modulations, Phys. Rev. B 62 (2000) 13707.
- [22] N. Israeli, H.-C. Jeong, D. Kandel, J.D. Weeks, Dynamics and scaling of one-dimensional surface structures, Phys. Rev. B 61 (2000) 5698.
- [23] M. Ozdemir, A. Zangwill, Morphological equilibration of a corrugated crystalline surface, Phys. Rev. B 42 (1990) 5013.
- [24] F. Lançon, J. Villain, Dynamics of a crystal-surface below its roughening transition, Phys. Rev. Lett. 64 (1990) 293.
- [25] J. Hager, H. Spohn, Self-similar morphology and dynamics of periodic surface profiles below the roughening transition, Surf. Sci. 324 (1995) 365.
- [26] H.P. Bonzel, E. Preuss, B. Steffen, The dynamical behavior of periodic surface profiles on metals under the influence of anisotropic surface-energy, Appl. Phys. A 35 (1984) 1.
- [27] H.P. Bonzel, E. Preuss, Morphology of periodic surface-profiles below the roughening temperature – aspects of continuum theory, Surf. Sci. 336 (1995) 209.
- [28] W. Burton, N. Cabrera, F. Frank, The growth of crystals and the equilibrium structure of their surfaces, Phil. Trans. Roy. Soc. London Ser. A 243 (1951) 299.
- [29] Z. Hu, S. Li, J.S. Lowengrub, Morphological stability analysis of the epitaxial growth of a circular island: application to nanoscale shape control, Physica D 233 (2) (2007) 151.
- [30] J. Krug, Four lectures on the physics of crystal growth, Physica A 313 (2002) 47.
- [31] A. Rätz, A. Voigt, Phase-field models for island dynamics in epitaxial growth, App. Anal. 83 (10) (2004) 1015.
- [32] F. Otto, O. Penzler, A. Rätz, T. Rump, A. Voigt, A diffuse interface approximation for step flow in epitaxial growth, Nonlinearity 17 (2004) 477–491.
- [33] F. Haußer, A. Voigt, Finite element method for epitaxial island growth, J. Crystal Growth 266 (2004) 381.
- [34] E. Bänsch, O. Lskkis, B. Li, F. Haußer, A. Voigt, Finite element method for epitaxial growth with attachment-detachment kinetics, J. Comput. Phys. 194 (2) (2004) 409.
- [35] E. Bänsch, F. Haußer, A. Voigt, Technical Report 36, Research Center Caesar, 2003.
- [36] Y.-M. Yu, R. Backofen, A. Voigt, A phase-field simulation of stripe arrays on metal bcc(100) surfaces, Phys. Rev. E 77 (2008) 051605.
- [37] Y.-M. Yu, A. Voigt, Directed self-organization of trench templates for nanowire growth, Appl. Phys. Lett. 94 (2009) 043108.
- [38] C. Ratsch, M.F. Gyure, R.E. Caflisch, et al., Level-set method for island dynamics in epitaxial growth, Phys. Rev. B 65 (2002) 195403.
- [39] F. Haußer, A. Voigt, Step meandering in epitaxial growth, J. Crystal Growth 303 (1) (2007) 80.
- [40] O. Pierre-Louis, C. Misbah, Y. Saito, J. Krug, P. Politi, New nonlinear evolution equation for steps during molecular beam epitaxy on vicinal surfaces, Phys. Rev. Lett. 80 (1998) 4221.
- [41] F. Gillet, O. Pierre-Louis, C. Misbah, Non-linear evolution of step meander during growth of a vicinal surface with no desorption, Eur. Phys. J. B 18 (2000) 519.
- [42] O. Pierre-Louis, G. Danker, J. Chang, K. Kassner, C. Misbah, Nonlinear dynamics of vicinal surfaces, J. Crystal Growth 275 (2005) 56.
- [43] R. Ghez, S.S. Iyer, The kinetics of fast steps on crystal surfaces and its application to the molecular beam epitaxy of silicon, IBM J. Res. Develop. 32 (1998) 804.
- [44] P. Smereka, Semi-implicit level set methods for curvature and surface diffusion motion, J. Sci. Comp. 19 (1-3) (2003) 439.
- [45] J.S. Kim, K. Kang, J.S. Lowengrub, Conservative multigrid methods for Cahn–Hilliard fluids, J. Comput. Phys. 193 (2004) 511.

- [46] S. Wise, J. Kim, J.S. Lowengrub, Solving the regularized, strongly anisotropic Cahn–Hilliard equation by an adaptive nonlinear multigrid method, *J. Comput. Phys.* 226 (1) (2007) 414.
- [47] U. Trottenberg, A. Schuller, C. Oosterlee, *Multigrid*, Academic Press, New York, 2005.
- [48] Z. Hu, *Phase-field Modeling of Thin Film Epitaxial Growth*, Ph.D Dissertation, University of California, Irvine, 2008.
- [49] G. Danker, O. Pierre-Louis, K. Kassner, C. Misbah, Interrupted coarsening of anisotropic step meander, *Phys. Rev. E* 68 (2003) 020601.
- [50] F. Haußer, A. Voigt, Geometric Ginzburg–Landau theory for faceted crystals in one dimension: from coarsening to chaos through a driving force, *Phys. Rev. E* 79 (2009) 011115.
- [51] F. Haußer, M.E. Jabbour, A. Voigt, A step-flow model for the heteroepitaxial growth of strained, substitutional, binary alloy films with phase segregation: I. Modeling, *SIAM Multiscale Model. Simul.* 6 (2007) 158.
- [52] D.H. Yeon, P.R. Cha, J.S. Lowengrub, A. Voigt, K. Thornton, Linear stability analysis for step meandering instabilities with elastic interactions and Ehrlich–Schwoebel barriers, *Phys. Rev. E* 76 (2007) 011601.
- [53] R.L. Pego, Front migration in the nonlinear Cahn–Hilliard equation, *Proc. R. Soc. Lond. A* 422 (1989) 261.
- [54] J. Kim, A continuous surface tension force formulation for diffuse-interface model, *J. Comput. Phys.* 204 (2005) 784.
- [55] J.J. Xu, H.K. Zhao, An eulerian formulation for solving partial differential equations along a moving interface, *J. Sci. Comp.* 19 (1–3) (2003) 573.